An evapotranspiration model self-calibrated from remotely sensed surface soil moisture, land surface temperature and vegetation cover fraction: application to disaggregated SMOS and MODIS data

Bouchra Ait Hssaine [1,2], Olivier Merlin [2], Jamal Ezzahar [3,4], Nitu Ojha [2], Salah Er-raki [4,5], and Said Khabba [1,4]

[1]LMME,Département de physique, Faculté des sciences Semlalia, Université Cadi Ayyad, Marrakech, Morocco
[2]CESBIO, Université de Toulouse, IRD/CNRS/UPS/CNES, Toulouse, France
[3]Département d'Informatique et Télécommunications, MTI, Ecole Nationale des Sciences Appliquées, Université Cadi Ayyad, Safi, Morocco
[4]CRSA, Centre for Remote Sensing Applications, University Mohammed VI Plytechnic (UM6P), BenGuerir, Morocco
[5]LP2M2E, Département de Physique Appliquée, Faculté des Sciences et Techniques, Université Cadi Ayyad, Marrakech, Morocco

Correspondence: Bouchra Ait Hssaine
(bouchraaithssaine@gmail.com)

Abstract. Thermal-based two-source energy balance modeling is essential to estimate the land evapotranspiration (ET) in a wide range of spatial and temporal scales. However, the use of thermal-derived land surface temperature (LST) is not sufficient to simultaneously constrain both soil and vegetation flux components. Therefore, assumptions (on either soil or vegetation fluxes) are commonly required. To avoid such assumptions, an energy balance model TSEB-SM was recently developed by
5 (Ait Hssaine et al., 2018b) in order to consider the microwave-derived near-surface soil moisture (SM), in addition to the thermal-derived LST and vegetation cover fraction (f_c) normally used. While TSEB-SM has been successfully tested using in-situ measurements, this paper represents its first evaluation in real-life using 1 km resolution satellite data, comprised of MODIS (Moderate resolution imaging spectroradiometer) for LST and f_c data and 1 km resolution SM data disaggregated from SMOS (Soil Moisture and Ocean Salinity) observations. The approach is applied during a four-year period (2014-2018)
10 over a rainfed wheat field in the Tensift basin, central Morocco . The field used was seeded for the 2014-2015 (S1), 2016-2017 (S2) and 2017-2018 (S3) agricultural season, while it remained not ploughed (as bare soil) during the 2015-2016 (B1) agricultural season. The classical TSEB model, which is driven only by LST and f_c data, significantly overestimates latent heat fluxes (LE) and underestimates sensible heat fluxes (H) for the four seasons. The overall mean bias values are 119, 94, 128 and 181 W/m^2 for LE and -104, -71, -128 and -181 W/m^2 for H, for S1, S2, S3 and B1, respectively. Meanwhile, when using
15 TSEB-SM (SM and LST combined data), these errors are significantly reduced, resulting in mean bias values estimated as 39, 4, 7 and 62 W/m^2 for LE and -10, 24, 7, and -59 W/m^2 for H, for S1, S2, S3 and B1 respectively. Consequently, this finding confirms again the robustness of the TSEB-SM to estimate latent/sensible heat fluxes at large scale by using readily available satellites data. In addition, the TSEB-SM approach has the original feature to allow for calibrating its main parameters (soil resistance and Priestley-Taylor coefficient) from satellite data uniquely, without relying neither on in-situ measurements nor
20 on a priori parameter values.

1

1 Introduction

Evapotranspiration (ET) is a crucial water flux in semi-arid areas (Bhattarai et al., 2019; Gerhards et al., 2019; Mallick et al., 2014, 2016) where it strongly impacts the drought monitoring, water resource management and climate (Littell et al., 2016; Molden et al., 2010). Furthermore, a precise estimate of ET determines the crop water requirements, which subsequently allows
5   the irrigation regimes to be optimized (Allen et al., 1998).

Regarding the data availability over extended areas, remote sensing is the only viable technique that can provide representative and multi-resolution measurements of ET. As a consequence, the spatial modelling has become a dominant means to estimate ET fluxes over regional and continental areas (Anderson et al., 2007; Fisher et al., 2017). In this context, numerous models based on land surface temperature (LST) data have been developed such as : (i) residual balance methods that consider
10 ET as the residual term of the energy balance like TSEB (Two-Source Energy Balance, (Norman et al., 1995)) and SEBS (Surface Energy Balance System, (Su, 2002)), (ii) contextual methods that estimate ET as the potential ET times the evaporative efficiency (Moran et al., 1994) or as the available energy times the evaporative fraction (Merlin et al., 2013; Roerink et al., 2000) and (iii) other categories of models that integrate LST into a water balance model (Olivera-Guerra et al., 2018) or into Penman-Monteith energy balance (PMEB) equation to directly estimate ET (Amazirh et al., 2017; Mallick et al., 2015).

15 Among well-known temperature-driven energy flux models, the TSEB model proposed by Norman et al. (1995) has been shown to be robust for a wide range of landscapes (Colaizzi et al., 2012; Ait Hssaine et al., 2018a). TSEB has two key input variables, which can be derived from remote sensing data. The first one is the LST and the second is vegetation cover fraction (f_c). The TSEB model adopts an iterative procedure, in which an initial estimate of the plant transpiration is given by the Priestly-Taylor (PT) formulation (Priestley and Taylor, 1972). This assumption requires few input data and allows a precise
20 estimate of potential ET (Fisher et al., 2008). Nevertheless, several studies (Ait Hssaine et al., 2018b; Fisher et al., 2008; Jin et al., 2011; Yang et al., 2015) have stressed that the PT coefficient cannot be considered as a constant value, as it is influenced by several parameters. Other authors (Gonzalez-dugo et al., 2009; Long and Singh, 2012; Morillas et al., 2014) reported that the PT approach may overestimate the canopy ET, especially for low soil wetness, and/or sparse vegetation cover, because it does not include a reasonable reduction of the initial canopy ET under stress conditions. Recently, Boulet
25 et al. (2015) have developed the Soil-Plant-Atmosphere and Remote Sensing Evapotranspiration (SPARSE) model similar to TSEB model in its basic assumption. Nevertheless, SPARSE is solved in two modes: the prescribed and the retrieval mode to constrain the output fluxes. The former first generates an equilibrium LST from the evaporation efficiency and the transpiration efficiency estimates by assuming that their values are equal to 1. Then, LST is implemented in the SPARSE retrieval mode to circumscribe the output fluxes by both limiting cases (namely the fully stressed and potential conditions). In spite of the good
30 retrieval performances of ET by this model significant uncertainties are observed during the quasi-senescent vegetation period (Boulet et al., 2015) .

Alternatively to the use of LST as a proxy for ET, numerous studies have stressed that the soil moisture plays a critical role in the partitioning of available energy into latent and sensible heat fluxes and is the prominent controlling factor of actual ET (Boulet et al., 2015; Gokmen et al., 2012; Kustas et al., 1998, 1999; Li et al., 2006). Several authors have revised the

well-known LST-based TSEB model and replaced the LST with microwave-derived surface soil moisture (SM) to estimate daily ET (Bindlish et al., 2001; Kustas et al., 1998, 1999; Li et al., 2006). Bindlish et al. (2001) found that the impact of SM on surface fluxes is strongly related to the vegetation cover. The impact is high for low fraction cover, and relatively weak for high cover fraction. Moreover, the soil evaporation is constrained by the SM through soil-texture dependent coefficients reported in (Sellers et al., 1992). In the same way, Li et al. (2006) indicated that the model performance is sensitive to these two coefficients, and thus they proposed to average the output of LST-based TSEB and SM-based TSEB models, in order to provide more consistent results over a wide range of conditions.

Previous studies, either LST- or SM-based, agree with the view that combining both LST and SM information at a time would enhance the robustness and accuracy of ET estimates in various biomes and climates. Nevertheless, few studies have simultaneously combined both observations in a unique energy balance model. One difficulty lies in developing a consistent representation of the soil evaporation (as constrained by SM, (Chanzy and Bruckler, 1993)), the total ET (as constrained by LST, (Norman et al., 1995)) and the plant transpiration (as indirectly constrained by both LST and SM, (Ait Hssaine et al., 2018b)).

Gokmen et al. (2012) explicitly integrated the SM derived from AMSR-E (Advanced Microwave Scanning Radiometer for EOS) data (Owe et al., 2008) into the LST-derived SEBS model via the kB-1 parameter, which plays an important role in the aerodynamic resistance. The updated SEBS model (SEBS-SM) provided a large improvement of sensible heat flux and thus ET estimates under water-limited conditions. The point is that the soil evaporation reduction parameters were calibrated using in-situ measurements, which limits the validity of the approach over large areas. In the same vein, Gan and Gao (2015) incorporated a SM-based soil resistance term in the TSEB formalism and calibrated several parameters (including the PT coefficient) using LST data. The obtained results showed that the model calibrated by LST data performed better than the non-calibrated one. Note that the parameters of the soil resistance were set to constant values as in Sellers et al. (1992) and Li et al. (2006). As a further step towards the combination of LST and SM data. Ait Hssaine et al. (2018b) modified the TSEB formalism (Kustas and Norman, 1999; Norman et al., 1995) (named TSEB-SM) and proposed a new calibration strategy of the main PT-based TSEB-SM parameters. The TSEB-SM model was tested using in-situ measurements and provided an important improvement in terms of latent heat flux/sensible heat flux estimates compared to the classic TSEB all along the agricultural season, especially during the crop emergence and the senescence periods. Such improvements are attributed to stronger constraints exerted on the representation of soil evaporation (via SM data and the calibrated soil parameters) and plant transpiration (via the calibrated daily PT coefficient). It should be noted that only LST and SM data are used for the calibration of yearly a_{rss} and b_{rss} as well as daily α_{PT}, while the flux measurements are needed only for the validation of the TSEB-SM simulated sensible and latent heat fluxes.

One crucial point is that all the above studies based on remotely sensed SM and LST have neglected the mismatch in the spatial resolutions of readily available SM products. Especially, the global scale SM data sets have a typical resolution of 40-50 km (Entekhabi et al., 2010; Kerr et al., 2010; Njoku et al., 2003). Such spatial resolution is generally unsuitable or even incompatible with many hydrological and agricultural applications. To fill the gap, disaggregation approaches of AMSR-E, SMOS (Soil Moisture and Ocean Salinity) and SMAP (Soil Moisture Active and Passive) like SM data have been developed

Peng et al. (2017) but, to date, there has been no application of SM-based ET models to disaggregate SM data sets. In addition, the use of remote sensing data would be necessary in order to avoid the time-consuming process of calibrating the TSEB model over each field.

TSEB-SM has the cutting edge capability to calibrate its main parameters from remotely sensed data, but the real-life application has not yet been tested. The objective of this paper is thus to demonstrate for the first time this capacity using disaggregated SMOS and MODIS (Moderate resolution imaging spectroradiometer) data. In this purpose, TSEB-SM is applied to 1 km resolution using MODIS LST/ f_c data and to SMOS SM data is applied. To make the SMOS data spatially consistent with MODIS data, the SMOS SM is disaggregated at 1 km resolution using the DisPATCh (DISaggregation based on Physical And Theoretical scale Change) algorithm (Malbéteau et al., 2016; Merlin et al., 2013; Molero et al., 2016). The proposed methodology is evaluated over a rainfed wheat field in the Tensift basin, central Morocco during four agricultural seasons (2014-2018).

2 Data description and methods

2.1 Site and in-situ data description

The study site is situated in the east (Sidi Rahal) of the Tensift basin in central Morocco (see Figure 1). The region is characterized by a semi-arid Mediterranean climate, with an average yearly precipitation of about 250 mm and an atmospheric evaporative demand around 1600 mm per year according to the FAO method (Allen et al., 1998; Jarlan et al., 2015). Soil is characterized by a fine texture with 47% of clay, 33% of loam and 18,5% of sand (Er-Raki et al., 2007). The experiment has been setting up in a rainfed wheat ("Bour") field since 2013 (Ali Eweys et al., 2017; Amazirh et al., 2018; Merlin et al., 2018). Located within a larger area occupied by rainfed wheat 'Bour'. This field was chosen to be representative at a scale of 1 km, thus enabling the comparison between 1 km resolution satellite-derived and localized in-situ measurements. The field was seeded in September 2014, September 2016 and September 2017 for the 2014-2015 (S1), 2016-2017 (S2) and 2017-2018 (S3) agricultural seasons, respectively. However, It was not ploughed(remained as bare soil) during the 2015-2016 (B1) agricultural season due to an unusual lack of precipitation in autumn-winter 2015 (Merlin et al., 2018) Table 1.

The field was instrumented by an Eddy covariance (EC) system at a 2-m height. EC tower includes a CSAT3 3D sonic anemometer that measures the wind and temperature fluctuations, and a krypton hygrometer KH20 that measures the concentration of water vapour. The EC tower is also equipped with a CNR1 radiometer (Kipp and Zonen) to measure the four components of the net radiation (Rn) with several heat flux plates (HFT3-L, Campbell Scientific Ltd) to measure the soil heat flux (G). Energy balance closure analysis indicated that the available energy (Rn-G) was generally higher than the EC measurements. The relative closure was about 68%, 76%, 79% and 79% for S1, S2, S3 and B1, respectively. The sensible and latent heat fluxes (H and LE) were finally corrected to force the closure of the energy balance by the Bowen's ratio method (Twine et al., 2000). LST is measured at the EC station by using two Apogee IRTS-P infrared radiometers, oriented downward and measuring the surface leaving radiance between 8 to 14 μm, set up at a 2-m height above ground. An estimate of LST is obtained by averaging both measurements. The soil water content is measured at various depths (5, 10, 20, 30, 50, 70 cm)

4

using Time Domain Reflectometry probes (model CS616) installed in a soil pit at the bottom of the EC tower. A weather station was set up nearby the studied field to measure air temperature, solar radiation, relative humidity, wind speed and rainfall at 30-minute time step.

2.2 Remote sensing data

2.2.1 MODIS

Three products from the MODIS sensor onboard Terra and Aqua satellites are used in this study: 1) MODIS Terra/Aqua Land Surface Temperature product ((MOD11A1/MYD11A1), 2) MODIS Terra Vegetation Indices product (MOD13A2) and 3) MODIS Albedo (combined Terra and Aqua) product (MCD43A3). All products are gridded in the Sinusoidal projection.

The MOD11A1 and MYD11A1 provide LST at 1 km spatial resolution under clear-sky conditions, derived from Terra and Aqua, respectively. Brightness temperature from bands 31 and 32 are used to derive LST through a generalized split-window algorithm. The MOD13A2 provides several vegetation indices at 1 km resolution. One particular vegetation index of interest in this study is $NDVI$, available at 16-day temporal intervals. This product is derived from bands 1 and 2 of the MODIS Terra satellite.

The obtained $NDVI$ is used to derive the leaf area index (LAI) via the following formulation (Wang et al., 2013):

$$LAI = \left(NDVI \times \frac{1 + NDVI}{1 - NDVI} \right)^{1/2} \tag{1}$$

The vegetation cover fraction is expressed as (Kustas and Norman, 1997):

$$f_c = 1 - \exp(-0.5 LAI) \tag{2}$$

Finally, the MCD43A3 product provides the surface albedo (α) at 500 m resolution every 16 days. The latter is generated from both Terra and Aqua products. In this work, the shortwave broadband α is used by integrating its value over the entire solar emission spectrum (0.3-5.0 μm). This value is obtained as a weighted average of the directional hemispherical reflectance (black-sky-α) and the bi-hemispherical reflectance (white sky α) using their two extreme values. The current α (called "blue sky") is a weighted average between these two extreme cases (Lewis and Barnsley, 1994). Herein, the percentages of 85% and 15% are used for the direct and diffuse lights, respectively.

2.2.2 SMOS

The SMOS mission measures the natural (passive) microwave radiation around the frequency of 1.4 GHz (L-band). It aims to monitor SM at a depth of about 3–5 cm with a spatial resolution of about 40 km and an accuracy better than 0.04 m^3/m^3 (Kerr et al., 2012). The revisiting time at the equator is 3 days for both ascending and descending passes, which are sun synchronous at 6 am and 6 pm respectively. The SMOS level-3 1-day global SM product (MIR CLF31A/D) posted on the ~ 25 km Equal Area Scalable Earth (EASE) version 1.0 grid is used as input to DisPATCh algorithm.

2.2.3 DisPATCh

The DisPATCh remote sensing algorithm combines the coarse scale microwave-retrieved SM with high-resolution optical/thermal data within a downscaling relationship to produce SM at higher spatial resolution. A detailed description of the algorithm can be found in (Merlin et al., 2012) and (Malbéteau et al., 2016). The LST is first decomposed into its soil and vegetation components, which allows the soil evaporation and plant transpiration to be estimated separately (Merlin et al., 2012). The revised soil temperature is then used to estimate the soil evaporative efficiency (SEE), which is defined as the ratio of actual to potential soil evaporation. Finally, DisPATCh converts the high-resolution optical-derived SEE fields into high-resolution SM fields given a semi-empirical SEE model and a first-order Taylor series expansion around the SMOS observation. In our application, we applied DisPATCh to 40 km resolution SMOS level-3 SM and 1 km resolution MODIS optical/thermal data to produce SM at a 1 km resolution (Molero et al., 2016). The input datasets are composed of: MODIS LST, MODIS $NDVI$ and the GTOPO Digital Elevation Model (DEM) used to correct LST for topographic effects (Malbéteau et al., 2016; Merlin et al., 2013).

2.3 Methods

2.3.1 TSEB-SM

The recently developed TSEB-SM is fully described in Ait Hssaine et al. (2018b). The equations and sub-equations used in TSEB-SM are provided in Table 2., the main equations are reminded below . The originality of TSEB-SM is to integrate SM observations in addition to LST and vegetation cover fraction data, in order to calibrate both the soil resistance to evaporation (constant parameters) and the PT coefficient on a daily basis. The model is based on the original TSEB formalism, meaning that the energy balance for vegetation is the same as in TSEB using the PT formula, although the soil evaporation is estimated as a function of SM using a soil resistance developed by Sellers et al. (1992). The use of the soil resistance formulation is justified by the fact that its main parameters (a_{rss}, b_{rss}) can be ajusted based on soil texture characteristics (Merlin et al., 2016) or by combining SM and LST data under bare (Merlin et al., 2018) or partially covered (Ait Hssaine et al., 2018b) soil conditions.

The vegetation latent heat flux (LEveg) is estimated via the PT formulation:

$$LE_{veg} = \alpha_{PT}.f_g.\frac{\triangle}{\triangle + \gamma}.R_{n,veg} \tag{3}$$

where α_{PT} is the PT coefficient, f_g the fraction of green vegetation,γ the psychometric constant ($\approx$67 Pa K^-1), $\triangle$ the slope of the relationship between saturation vapor pressure and air temperature, and $R_{n,veg}$ is the vegetation net radiation. Note that, f_g is set to 1 as the α_{PT} coefficient is varied (through the calibration procedure) to take into account the fraction of transpiring vegetation. The soil latent heat flux is estimated using the resistance formulation:

$$LE_{soil} = \frac{\rho c_p}{\gamma}\frac{e_s - e_a}{r_{ah} + r_s + r_{ss}} \tag{4}$$

where e_s is the saturated vapor pressure at the soil surface, e_a the actual air vapor pressure, r_{ah} the aerodynamic resistance to heat transfer across the canopy–surface layer interface, r_s the resistance to heat flux in the boundary layer immediately above the soil surface, and r_{ss} the resistance to vapor diffusion and capillary flux in the soil. r_{ss} is computed as a function of SM and is expressed as (Chirouze et al., 2014; Li et al., 2006; Sellers et al., 1992):

$$r_{ss} = \exp(a_{rss} - b_{rss} \times \frac{SM}{SM_{sat}}) \tag{5}$$

with SM being the 0–5 cm SM, a_{rss} and b_{rss} are two empirical parameters (to be calibrated) and SM_{sat} is the SM at saturation expressed as (Cosby et al., 1984):

$$SM_{sat} = 0.1 \times (-108 \times f_{sand} + 49.305) \tag{6}$$

with f_{sand} being the sand percentage of soil.

In Ait Hssaine et al. (2018b), an innovative calibration approach of α_{PT}, a_{rss} and b_{rss} is developed from in-situ SM and LST data (Ait Hssaine et al., 2018b).The calibration methodology is briefly reminded below.

2-3-1-1 Retrieval and calibration of r_{ss}, a_{rss} and b_{rss}

The r_{ss} is first adjusted by minimizing a cost function defined by:

$$F_{inst} = (T_{surf,sim} - T_{surf,mes})^2 \tag{7}$$

With $T_{surf,sim}$ and $T_{surf,mes}$ being the simulated and measured LST, respectively. The inverted r_{ss} is then correlated to the SM (in-situ or DisPATCh) to determine the a_{rss} and b_{rss} parameters by considering that, when f_c is lower than a given threshold ($f_{c,thres}$), the dynamics of total LE is mainly controlled by the temporal variation of soil evaporation. Meaning that both soil parameters are estimated when the PT coefficient can be set to a constant value.'

2-3-1-2 Daily α_{PT} retrieval

Once the soil resistance has been calibrated, the PT coefficient is retrieved on a daily basis when f_c is larger than $f_{c,thres}$, by minimizing a cost function at the Terra and Aqua-MODIS overpass times:

$$F_{daily} = \sum (T_{surf,sim} - T_{surf,mes})^2 \tag{8}$$

In fact, an iterative loop is run on soil (r_{ss}) and vegetation (α_{PT}) parameters to reach convergence of all parameters. LST and SM data are thus used for calibration, while the calibrated TSEB-SM is run on a daily basis using SM data as forcing solely (in addition to vegetation cover fraction data). In this paper, an improvement is made on the former version of TSEB-SM to normalize the output fluxes using the LST-derived available energy. Therefore, the new version of TSEB-SM uses both LST and SM data (in addition to vegetation cover fraction data) as forcing on a daily basis. In practice, the latent and sensible heat fluxes derived from the TSEB-SM model are re-computed using the TSEB-SM derived evaporative fraction (EF, defined as the ratio of latent heat to available energy) and the LST-derived available energy. The rationale is that numerous modelling studies have shown the regularity and constancy of EF during daylight hours in cloud-free days (Gentine et al., 2011; Lhomme and

Elguero, 1999; Shuttleworth et al., 1989) and the EF has a strong link with SM availability (Bastiaanssen and Ali, 2003), which is an important factor for estimating latent heat flux. For that purpose, the LST data collected at the Terra and Aqua-MODIS overpass times are used separately to estimate the instantaneous R_n and G. A ratio between the daily (obtained as an average value between Aqua and Terra overpass times) latent heat flux LE_{daily} and the daily available energy ($R_{n,daily}$-G_{daily}) is used

5   to calculate an average daily EF:

$$EF = \frac{LE_{daily}}{R_{n,daily} - G_{daily}} \tag{9}$$

The daily EF and the instantaneous available energy (calculated using Terra and Aqua MODIS LST, separately) are finally used to re-calculate the instantaneous TSEB-SM output of LE and H by the following formulas:

$$LE = EF \times (R_n - G) \tag{10}$$

10

$$H = (1 - EF) \times (R_n - G) \tag{11}$$

2.3.2   Uncertainty in TSEB-SM input data

The LST collected by MODIS at Terra and Aqua overpass times and the SM product derived at 1 km resolution from the DisPATCh algorithm applied to SMOS data, are used as input to TSEB and TSEB-SM models. Validation of TSEB and TSEB-

15   SM input data prior to the evaluation of models output is an important issue, because of the scale discrepancy between the spatial resolution (1 km) of MODIS/DisPATCh data and the footprint of the EC flux measurements that does not exceed 100 m (Schmid, 1994).

    Several studies have demonstrated the effectiveness of DisPATCh 1km resolution SM. Malbéteau et al. (2016) compared DisPATCh SM data with the in-situ measurements collected in the Murrumbidgee catchment in Southeastern Australia. Their

20   results showed that DisPATCh improved the spatial representation of SM at 1 km resolution (compared to the original 40 km resolution SMOS SM), especially in semi-arid areas. Recently, Malbéteau et al. (2018) combined the DisPATCh SM over the entire year 2014 (Sidi Rahal-Morocco) with the continuous predictions of a surface model in order to obtain a better estimate of daily SM at 1 km resolution. They found that the assimilation of DisPATCh data improved quasi systematically the dynamics of SM.

25   Figure 2 shows the scatter plots of MODIS LST (at Terra and Aqua overpass) versus in-situ measurements for the four agricultural seasons separately. The obtained R^2, $RMSE$, and MBE are reported in Table 3. The statistical comparison shows strong linear correlations ($0.76 \leq R^2 \leq 0.90$) for all years. The $RMSE$ is around 4 K for S2 (2016-2017) and S3 (2017-2018) agricultural seasons while it reaches 6 K for S1 (2014-2015) and B1 (2015-2016), respectively. The observed scatter may stem from the fact that the localized (1 or 2 m wide) in-situ LST is not fully representative of the 1 km resolution MODIS

30   pixel (Ait Hssaine et al., 2018a; Yu et al., 2017). For all years (S1-3, B1), it can be seen that the MBE is negative. Note that the MBE is the greatest when the temperatures are largest. Such a systematic error is probably due to the non-representativeness of the in-situ LST observations when compared to the corresponding scale of MODIS observations.

In order to evaluate the 1 km resolution SM during the study period, Figure 3 shows a comparison of DisPATCh SM with in-situ measurements for the four wheat agricultural seasons (S1, B1, S2 and S3) separately. The statistical results including the coefficient of determination (R^2), the root mean square error ($RMSE$), and the mean bias error (MBE) are reported in Table 3. The R^2 ranges from 0.27 to 0.55, the $RMSE$ from 0.04 to 0.09 m^3/m^3 and the MBE from -0.05 to -0.03 m^3/m^3. These results are encouraging considering the heterogeneous land use composed of rainfed wheat, bare soil, fallow and farm building (see Figure 4) . In fact the localized in-situ measurements may not be perfectly representative of the 1 km resolution satellite data. Note that the efficiency of DisPATCh is supposedly higher for low SM values (Malbéteau et al., 2016), which is clearly illustrated during B1 season, while it is lower for high SM values (after rain events). This can be explained by the constraints of atmospheric and vegetation conditions on disaggregation results, as well as the saturation of SEE in the higher SMSM range. Another major issue that can lead to differences between DisPATCh and in-situ SM is that the ground SM sensors are buried at a depth of 5 cm while the penetration of the L-band wave varies between 2 and 5 cm depending on soil conditions (notably SM content, texture). For S2, the SM provided by DisPATCh underestimated field measurements, especially in the higher SM range. This particular behaviour could be explained by the particularly low precipitation amount during this year. Especially, it is possible that the surrounding plots were not sown by neighbour farmers, resulting in a soil that dried quickly compared to our field, which retained the SM for a longer period of time.

Note that despite the relative heterogeneity within the 1 km pixel (characterized by rainfed wheat in addition to bare soil and fallow), the comparison between field measurements and 1 km resolution satellite data reflects acceptable accuracies.

3   Results and Discussion

In this section, the a_{rss} and b_{rss} parameters and the α_{PT} are firstly retrieved by following the two-step calibration based on a threshold of f_c (cited in method's section). Then, the obtained calibrated values are used to estimate the surface fluxes using TSEB-SM. Finally, TSEB-SM fluxes are evaluated against the eddy covariance measurements, and results are compared with the original TSEB. To facilitate the interpretation of the simulation results using MODIS and SMOS/DisPATCh data as input, the calibration and validation steps are previously tested using in-situ (LST and SM) data.

3.1   Retrieving a_{rss} and b_{rss} parameters

The soil resistance r_{ss} is inverted for $f_c \leq f_{c,thres}$, between 11 am and 2 pm and at Terra and Aqua overpass time step for in-situ and satellite data, respectively. The result of this inversion is correlated to the actual to saturated soil moisture ratio SM/SM_{sat} to determine a_{rss} and b_{rss} parameters. The calibration process is applied for each season independently. Then a pair (a_{rss}, b_{rss}) is calculated for the entire study period for in-situ and satellite data, respectively.

Figure 5a and 5b plot the $\log(r_{ss})$ versus in-situ SM/SM_{sat} using in-situ and satellite data, respectively. The mean retrieved values (7.62, 2.43) and (7.32, 4.58) for in-situ and satellite data, respectively, are close to the values found in Li et al. (2006) (8.2, 4.3) and in Ait Hssaine et al. (2018b) (7.2, 4). However, by comparing both figures (5a and 5b), one notes that the use of in-situ data generates more scatter than with satellite data. The apparent scatter in retrieved r_{ss} could be interpreted by

the impact of the daily cycle of meteorological (evaporative demand) conditions or soil properties differences (Merlin et al., 2011, 2016, 2018). The retrieved soil parameters also vary from year to year: the standard deviation is 0.39 and 1.69 for a_{rss} and b_{rss}, respectively. This can be explained by the compensation effects linking a_{rss} and b_{rss} parameters which prove the empirical nature of the r_{ss}. Another major issue that can lead to these differences is the depth of SM measurements (Merlin

5　et al., 2011). In Sellers et al. (1992), the near-surface soil moisture is defined in the 0-5-cm soil layer, whereas in our field, SM measurements are made at 5-cm depth. Also, the sensing depth of SMOS observations is generally shallower than the in-situ surface measurements (Escorihuela et al., 2010). Moreover, the variability of a_{rss} and b_{rss} in Figure 5b using remote sensing data can be linked to the scale difference between DisPATCh SM/MODIS products (1 km) and the field measurements. As shown in Figure 3, the field is surrounded by trees, buildings and fallows, which causes the spatial heterogeneity within the

10　pixel of 1 km. This heterogeneity can introduce errors on the model inversion. Nevertheless, soil parameters are quite similar for in-situ and satellite data sets. Therefore, the heterogeneity issues within the 1 km pixel scale are minor in this study.

3.2　Time series of daily retrieved α_{PT}

The second calibration step consists in inverting the daily α_{PT} when vegetation is covering a significant part of soil ($f_c > f_{c,thres}$), for the three seasons of rainfed wheat (S1, S2 and S3), by using in-situ data and satellite data, separately. Herein, the

15　calibration of α_{PT} is bounded by a minimum (0) and maximum (2) acceptable physical value, in order to avoid unacceptable values of α_{PT} that can be produced because of the uncertainties in daily LST estimates. Such an upper bounding is especially needed when vegetation partially covers the soil.

3.2.1　Using in-situ data

Figure 6 plots the daily variation of α_{PT} for each season (S1, S2 and S3) separately, using in-situ data. The mean retrieved

20　values of α_{PT} are 1.26, 1.12 and 1.09 for S1, S2 and S3 respectively. In all cases, the mean α_{PT} is close to the theoretical α_{PT} value (1.26). It is well observed that the retrieved α_{PT} for S1 is slightly larger compared to those obtained for both S2 and S3. This can be explained by the timing and amount of rainfall during each season. Note that unexpected low values of α_{PT} are recorded for S3 during the first few days (25 January-4 March) of the development stage. They may be associated with uncertainties in retrieved α_{PT} as the impact of soil surface is still significant, as well as to a relatively low evaporative demand

25　especially since this period coincides with cloudy days and abundant precipitations. Indeed, the coupling between transpiration (and hence retrieved α_{PT}) and LST is expected to be lower under lower atmospheric demand.

　　The retrieved α_{PT} is then smoothed as in Ait Hssaine et al. (2018b) to remove outliers and to reduce uncertainties at the daily time scale. The smoothed values of α_{PT} range from 0 to 1.54, 0 to 1.38 and 0.45 to 1.43 for S1, S2 and S3 respectively. The maximum of α_{PT} is close to 1.26 for S2, while it is higher for S1 and S3. This result is in accordance with the total rainfall

30　amounts which were about 608, 214 and 421 mm for S1, S2 and S3 respectively. Additionally, one can state that the stability of α_{PT} strongly depends on the rainfall distribution along the agricultural season. The daily α_{PT} is more stable for S1 than for S2 and S3. Indeed, the amount of rain during S1 is very important with two peaks of about 83 mm that occurred at the beginning of the season and during the growing stage. The second one coincides exactly with the maximum value of the retrieved α_{PT}.

However, different results are obtained for S2 compared to S1 due to the lowest precipitation amount recorded over that season. As shown in Figure 6 the amount of rain is concentrated at the beginning of the growing stage (mid December), when the α_{PT} peaks. Afterward, the smoothed α_{PT} tends to decrease because of insufficient soil water reserve in the root zone to enable wheat to continue growing. Rainfall is also significant for S3 and every rainfall event causes an immediate (daily) response of α_{PT} (after 4th March). As mentioned before, the significant error in α_{PT} retrievals for S3 between 25 January and 4 March induces strong uncertainties in the smoothing function estimates.

3.2.2 Using satellite data

Figure 6 illustrates also the daily variation of α_{PT} retrieved from satellite data for each season separately. S1 and S2 have a very similar distribution of the retrieved α_{PT} as compared to the retrieved α_{PT} using in-situ data, respectively. For S3, only six retrieved α_{PT} values are available because of the non-availability of MODIS products during cloudy days. For this reason, no information linked to the variability of α_{PT} can be derived during this season. The retrieved values are smoothed and superimposed with the rainfall events. It is clearly shown that the smoothed α_{PT} for S1 and S2 have the same shape with a small variability, when comparing with the smoothed α_{PT} using in-situ data, resulting in an error estimated as the $RMSE$ to the mean α_{PT} ratio, of about 11 and 19 %, for S1 and S2 respectively. For S1 the maximum of smoothed α_{PT} is reached at the same time as when using the in-situ data, with a value of about 1.38, while the maximum for S2 is reached 10 days before the maximum of the α_{PT} derived from in-situ data with little response of α_{PT} to rainfall events. These differences may be linked to uncertainties in disaggregated SMOS SM, as well as to the weaker availability of satellite data. Because of the small number of data points (retrieved α_{PT}) during S3, the smoothed α_{PT} remains at a mostly constant value (~ 0.7) throughout the study period, with a significant relative difference of about 34 % when comparing with the α_{PT} retrieved using in-situ data.

3.2.3 Interpretation of α_{PT} variabilities

Figure 7 plots variation of calibrated daily α_{PT}, superimposed with $NDVI$ and rainfall events. It is visible that the maximum value of $NDVI$ appears sooner than the maximum value of α_{PT} for both S1 and S3. Such a delay is attributed to the high soil moisture level in the root-zone during the maturity stage. Later in the season, α_{PT} decreases as $NDVI$ starts to decline at the onset of senescence. In contrast, the maximum value of $NDVI$ appears later than the maximum value of α_{PT} for S2. This can be explained by the fact that rainfall at the beginning of the development phase satisfies the plant requirements, while the rainfall amount during the development stage is relatively low compared to the crop water needs (Kharrou et al., 2011). Large variations in α_{PT} occur during the agricultural season, as a result of the amount, frequency, and distribution of rainfall along the season. In general, the analysis of the α_{PT} variability using satellite data illustrates the robustness of the proposed approach, which combines microwave and optical/thermal data to retrieve a water stress indicator at the daily time scale.

3.3 Surface fluxes

The robustness of TSEB and TSEB-SM for partitioning $(R_n - G)$ into H and LE is evaluated using in-situ and remotely sensed LST,SM, NDVI, separately, at Terra and Aqua MODIS overpasses.

3.3.1 Using in-situ data

5 Figure 8 shows an intercomparison of simulated and observed LE for the 4 seasons separately. TSEB-SM clearly provides improved results compared to the original TSEB. The obtained values of $RMSE$ by TSEB-SM are about 68 and 72 W/m^2 for S1 and S2 respectively, which is significantly lower than those revealed by TSEB (109 and 86 W/m^2, respectively) (see Table 4). For B1 (season of bare soil), TSEB largely overestimates LE with a MBE of about 165 W/m^2 compared to TSEB-SM, which yields a MBE of 59 W/m^2. This overestimation of TSEB is most probably related to an inadequate value of α_{PT}

10 (=1.26) for bare soil surfaces. In fact, 1.26 is an optimum value for the potential transpiration rate (Agam et al., 2010; Chirouze et al., 2014). In the case of TSEB-SM, biases are reduced thanks to the calibration of the r_{ss} resistance. Additionally, according to TSEB-SM assumptions, α_{PT} for $f_c \leq 0.5$ is set to the average value of the α_{PT} retrieved for $f_c > 0.5$. During B1 season (bare soil conditions), α_{PT} was hence obtained as an average value of the mean α_{PT} retrieved for all seasons S1, S2 and S3 when $f_c > 0.5$ ($\alpha_{PT} \sim 1$). However, this value remains relatively high for a bare soil, which yields a slight overestimate of

15 LE measurements (see B1 case in Figure 8).

For S3 season, the error on daily retrieved α_{PT} at the beginning of the development stage has a strong impact on LE predictions and thus yields to greater discrepancies illustrated in Figure 8. To overcome this error, the threshold on f_c to separate calibration steps 1 and 2 was increased to 0.63 (arbitrary value). The TSEB-SM model is then run using the new threshold. The LE simulations are improved, with a $RMSE$ of 73 W/m^2 instead of 98 W/m^2 and a relative error (estimated

20 as the $RMSE$ divided by the mean observed LE) of about 42 % instead of 58 %. The increase in the threshold is intended to decrease the uncertainties in α_{PT} retrievals when vegetation is not fully covering the soil. It can be concluded that the errors in α_{PT} retrievals have a strong impact on LE estimates.

The ability of TSEB-SM to estimate the sensible heat fluxes is also investigated. Figure 9 displays the comparison between TSEB and TSEB-SM for each season and Table 4 summarized the different statistical parameters. One can notice that TSEB

25 shows greater discrepancies in H estimation, with a $RMSE$ of about 127, 112 and 103 W/m^2 and MBE of about -41, 1, and -71 W/m^2 for S1, S2 and S3 respectively. Both $RMSE$ and MBE values are generally much reduced when using TSEB-SM with $RMSE$ values of about 68, 72, and 98 W/m^2 and MBEMBE values of about -10, 24, and 7 W/m^2, respectively. During B1, TSEB model underestimates H. This can be explained by the low-sensitivity of simulated sensible heat flux to changes in surface and atmospheric conditions, consistent with former results obtained on a different sites of irrigated wheat (Ait Hssaine

30 et al., 2018b). The discrepancies between TSEB-SM and in-situ H during S3 are mostly rectified by using the new threshold on f_c: the statistical results are improved, the $RMSE$ is about 73 W/m^2 and the relative error is 39 % (instead of 52 %). It can be concluded that the uncertainty observed over the α_{PT} during the first few days of development stage (25 January-4 March) is mainly related to the impact of the soil, which is not negligible during the first weeks of the growing stage. Nevertheless, by

considering the overall results obtained for the 3 seasons, the threshold of $f_{c,thres} = 0.5$ can be considered as an acceptable value to calibrate the soil resistance parameters and the Priestly Taylor coefficient.

As a further step, the intercomparison between TSEB and TSEB-SM is evaluated by predicting R_n and G fluxes instead of forcing them to their measured values. The statistical results of the comparison between simulated and observed R_n, G,H and
5   LE are listed in Table 5. The scattering obtained when comparing turbulent flux estimations to measurements is mainly related to the uncertainty in available energy estimates, mainly related to the uncertainty in soil heat flux estimates. Indeed, as reported in Table 5, R_n is very well simulated for both TSEB and TSEB-SM. The R^2 between simulated and observed R_n is about 0.99 during all seasons. Meanwhile G shows a poor correlation, with an R^2 varying from 0.05 to 0.45. This is mainly linked to the approach used to estimate G, which requires local calibration. Kustas et al. (1998) hence indicated that the ratio G/$R_{n,soil}$
10 cannot be considered as a constant, because it is affected by different factors such as time of day, moisture conditions and soil texture and structure.

3.3.2   Using satellite data

In order to gain greater insight into how TSEB and TSEB-SM models respond to different surface conditions across a landscape, an analysis of the spatial distributions and the magnitude of the turbulent fluxes using remotely sensing data produced from the
15 two models is conducted. The comparisons between TSEB/TSEB-SM versus observed LE over the four seasons are illustrated in Figure 10.Figure 10 indicates that TSEB overestimates latent heat flux. The overall MBE are about 119, 181, 94 and 128 W/m^2 for S1, B1, S2 and S3 respectively. The overestimation of LE fluxes can be explained by the fact that α_{PT} is set to 1.26 during the entire agricultural season including stress conditions. This probably causes larger errors on the LE estimation especially during the growing stage. Indeed, the saturation of TSEB during the senescence period is precisely caused by the
20 PT coefficient fixed to 1.26. The errors are reduced when using TSEB-SM. In fact, the constraint on plant transpiration, while retrieving daily α_{PT} values improves ET estimates especially for the growing stage. Moreover, during the senescence stage the large positive bias of LE is considerably reduced. In fact, the decrease in calibrated daily α_{PT} is associated with the drop in NDVI during senescence (Ait Hssaine et al., 2018b). Additionally, the constraint on the soil evaporation via the DisPATCh SM, clearly reduces the MBE values during the emergence period ($f_c \leq f_{c,thres}$). Finally, the constraint applied on TSEB-SM
25 output fluxes using LST-derived available energy and TSEB-SM-derived evaporative fraction (Equation 8) improves the LE estimates for the whole study period. The MBE are about 39, 4, 7 and 62 W/m^2 for S1, S2, S3 and B1 respectively.

TSEB consistently exhibits larger errors on H estimation (see Figure 11), with $RMSE$ values up to 98, 73, 56 and 66 W/m^2 during S1, S2, S3 and B1 respectively. The $RMSE$ is improved while using TSEB-SM, with values of about 55, 41, 24 and 27 W/m^2 during S1, S2, S3 and B1 respectively.
30 The intercomparison between TSEB and TSEB-SM is made by forcing the available energy to its measured value. The statistics listed in Table 5 indicate that there are similar differences between modeled versus measured R_n using either TSEB or TSEB-SM. Overall, the discrepancies between estimated and measured R_n are likely due to a greater scatter between MODIS and in-situ measured LST. Note that $RMSE$ values up to 6 K have been noted when comparing LST MODIS with ground-based measurements. These uncertainties are likely to be explained by the huge scale mismatch between the 1 km resolution

of MODIS LST and the footprint size (approximately 1 m) of ground-based radiometers. The uncertainties in key input data generate large differences in simulated R_n compared to the tower measurements. The greater scatter between modeled and measured G from the two models reflect the fact that there is a major mismatch in scale between the area sampled by the soil heat flux sensors and the 1 km resolution of model inputs. It appears that the LE estimates from TSEB-SM are generally in closer agreement with the measurements than the TSEB model outputs. The $RMSE$ is significantly improved from 103 to 52 W/m^2, from 151 to 30 W/m^2, from 101 to 35 W/m^2 and from 83 to 24 W/m^2, during S1, B1, S2 and S3, respectively. For the sensible heat flux H, the difference between TSEB estimates and EC measurements listed in Table 5 indicates a fairly large underestimation, the MBE values varying between -56 W/m^2 and -240 W/m^2. However, the TSEB-SM output provides a quite significant improvement, with an absolute MBE lower than -61 W/m^2 during all seasons.

3.4   Evaluation of H and LE estimates

In this section, the residual error of the H and LE estimated with the TSEB-SM retrieved soil/vegetation parameters is analyzed. Figure 12 plots retrieved α_{PT} vs residual H and LE error. The retrieved α_{PT} is poorly correlated to residual H (R=-0.27) and ET (R=0.27) errors especially for the seasons S1 and S2. For the season S3, few retrieved α_{PT} values were available because of the non-availability of MODIS products during cloudy days. It is shown that the trend between α_{PT} and residual H error is slightly negative for S1 while it is slightly positive for S2. According to these results, no information linked to the variability of α_{PT} versus residual ET and H errors can be derived. Figure 13 plots retrieved r_{ss} vs residual H and LE error and LST for the four study periods. The retrieved r_{ss} is negatively correlated (R=-0.33) with residual H error (predicted–observed) for the four seasons, while it is positively correlated (R=0.33) with residual LE error. The residual error covers a wide range (between -150 and 150 W/m^2) for the lower r_{ss} values, while it is biased for the higher r_{ss} values. Such a result indicates that the r_{ss} formulation as a function of near-surface SM needs further improvements (Merlin et al., 2016, 2018) in order to reduce systematic uncertainties in evaporation estimates, especially in dry (moisture-limited) conditions. Consistent with the general decrease of LST with SM, LST is positively correlated to retrieved r_{ss} (R=0.45). This is very coherent since r_{ss} decreases with the increase of SM. Regarding the sensitivity analysis of residual H and LE errors to observed SM, Figure 14 shows that SM is positively correlated with residual H error, while it is negatively correlated with residual LE error for the entire study period. The correlation coefficient is about 0.3 when using DisPATCh SM while it is about 0.4 when using in-situ SM. This difference can be explained by the uncertainty (including spatial representativeness issues at the localized scale) in DisPATCh SM. The positive correlation coefficient between residual LE error and observed SM is likely to be due to the systematic errors in r_{ss} estimates for dry conditions as mentioned previously. For S2, B1 and S3, the residual H error ranges between -150 and 50 W/m^2 for SM between 0-0.10 m^3/m^3 while it is slightly overestimated for the higher range of SM. The residual LE error is also found to be influenced by SM, but in the opposite sense.

4 Conclusions

The microwave-derived near-surface soil moisture (SM) from SMOS and thermal-derived land surface temperature (LST) from MODIS are integrated simultaneously within a calibration procedure to invert both the soil resistance to evaporation (constant parameters) and the PT coefficient based on a threshold on f_c. The TSEB-SM model is applied during a four-year period (2014-2018) over a rainfed wheat field in the Tensift basin, central Morocco. The first calibration step with $f_c \leq f_{c,thres}$ consists in inverting r_{ss} at Terra and Aqua overpass times. Despite the scale difference between the MODIS/DisPATCh resolution data and the footprint size of in-situ measurements, the pair parameters (a_{rss}, b_{rss}) calculated for the entire study period using satellite data are relatively close to those derived from in-situ measurements. The second calibration step consists in estimating α_{PT} on a daily basis for $f_c > f_{c,thres}$ by using LST and SM data. The maximum of daily calibrated α_{PT} are 1.38, 1.25 and 0.87, when using satellite data, for S1, S2 and S3, respectively. Those values are in accordance with the total rainfall amounts, which were about 608, 214 and 421mm/wheat season for S1, S2 and S3 respectively. S1 and S2 have the same distribution of daily calibrated α_{PT} when comparing with the α_{PT} retrieved using in-situ data, while the retrieved α_{PT} remains at a mostly constant value (~ 0.7) throughout the study period S3 because of the non-availability of MODIS products during cloudy days.

An analysis of the spatial distributions and the magnitude of the turbulent fluxes using remotely sensing data produced from the two models were conducted. TSEB exhibits larger errors on H and LE estimates. These uncertainties can be linked to the theoretical value of α_{PT}, which is fixed to 1.26 for the whole study period, as well as to the scale mismatch between the 1 km resolution of MODIS LST and the footprint size (approximately 1 m) of the ground-based radiometer. The constraint applied on the soil evaporation represented explicitly as a function of SM via a soil resistance term reduces the errors when using TSEB-SM. In fact, the use of the SM derived from microwave data is one of the main controlling factors of the evaporative fraction, which helps to determine with more accuracy the LE/H partitioning.

Last but not least, the coupling of the soil resistance formulation with the TSEB formalism improves the estimation of soil evaporation, and should, as a consequence, improve the partitioning of evapotranspiration. As a short term prospect, the robustness of TSEB-SM in terms of evaporation/transpiration partitioning will be tested by using independent flux measurements derived from lysimeters, and sap flow sensors, and vapour chambers (Rafi et al., 2019).

References

Agam, N., Kustas, W. P., Anderson, M. C., Norman, J. M., Colaizzi, P. D., Howell, T. A., Prueger, J. H., Meyers, T. P., and Wilson, T. B.: Application of the Priestley–Taylor Approach in a Two-Source Surface Energy Balance Model, Journal of Hydrometeorology, 11, 185–198, https://doi.org/10.1175/2009JHM1124.1, http://journals.ametsoc.org/doi/abs/10.1175/2009JHM1124.1, 2010.

5 Ait Hssaine, B., Ezzahar, J., Jarlan, L., Merlin, O., Khabba, S., Brut, A., Er-Raki, S., Elfarkh, J., Cappelaere, B., and Chehbouni, G.: Combining a Two Source Energy Balance Model Driven by MODIS and MSG-SEVIRI Products with an Aggregation Approach to Estimate Turbulent Fluxes over Sparse and Heterogeneous Vegetation in Sahel Region (Niger), Remote Sensing, 10, 974, https://doi.org/10.3390/rs10060974, http://www.mdpi.com/2072-4292/10/6/974, 2018a.

Ait Hssaine, B., Merlin, O., Rafi, Z., Ezzahar, J., Jarlan, L., Khabba, S., and Er-Raki, S.: Calibrating an evapotranspiration model using
10 radiometric surface temperature, vegetation cover fraction and near-surface soil moisture data, Agricultural and Forest Meteorology, 256-257, 104–115, https://doi.org/10.1016/j.agrformet.2018.02.033, 2018b.

Ali Eweys, O., José Escorihuela, M., Villar, J. M., Er-Raki, S., Amazirh, A., Olivera, L., Jarlan, L., Khabba, S., and Merlin, O.: remote sensing Disaggregation of SMOS Soil Moisture to 100 m Resolution Using MODIS Optical/Thermal and Sentinel-1 Radar Data: Evaluation over a Bare Soil Site in Morocco, Remote Sensing, 9, 1155, https://doi.org/10.3390/rs9111155, www.mdpi.com/journal/remotesensing, 2017.

15 Allen, R. G., Pereira, L. S., Raes, D., and Smith, M.: Crop evapotranspiration-Guidelines for computing crop water requirements-FAO Irrigation and drainage paper 56, Tech. rep., https://appgeodb.nancy.inra.fr/biljou/pdf/Allen{_}FAO1998.pdf, 1998.

Amazirh, A., Er-Raki, S., Chehbouni, A., Rivalland, V., Diarra, A., Khabba, S., Ezzahar, J., and Merlin, O.: Modified Penman–Monteith equation for monitoring evapotranspiration of wheat crop: Relationship between the surface resistance and remotely sensed stress index, Biosystems Engineering, 164, 68–84, https://doi.org/10.1016/j.biosystemseng.2017.09.015, https://doi.org/10.1016/j.biosystemseng.
20 2017.09.015, 2017.

Amazirh, A., Merlin, O., Er-Raki, S., Gao, Q., Rivalland, V., Malbeteau, Y., Khabba, S., and Escorihuela, M. J.: Retrieving surface soil moisture at high spatio-temporal resolution from a synergy between Sentinel-1 radar and Landsat thermal data: A study case over bare soil, Remote Sensing of Environment, 211, 321–337, https://doi.org/10.1016/j.rse.2018.04.013, http://linkinghub.elsevier.com/retrieve/pii/S0034425718301585, 2018.

25 Anderson, M. C., Norman, J. M., Mecikalski, J. R., Otkin, J. A., and Kustas, W. P.: A climatological study of evapotranspiration and moisture stress across the continental United States based on thermal remote sensing: 2. Surface moisture climatology, JOURNAL OF GEOPHYSICAL RESEARCH, 112, D11 112, https://doi.org/10.1029/2006JD007507, https://naldc.nal.usda.gov/download/59923/PDF, 2007.

Bastiaanssen, W. G. and Ali, S.: A new crop yield forecasting model based on satellite measurements applied across the Indus Basin, Pakistan,
30 Agriculture, Ecosystems & Environment, 94, 321–340, https://doi.org/10.1016/S0167-8809(02)00034-8, http://linkinghub.elsevier.com/retrieve/pii/S0167880902000348, 2003.

Bhattarai, N., Mallick, K., Stuart, J., Vishwakarma, B. D., Niraula, R., Sen, S., and Jain, M.: An automated multi-model evapotranspiration mapping framework using remotely sensed and reanalysis data, Remote Sensing of Environment, 229, 69–92, https://doi.org/10.1016/j.rse.2019.04.026, https://doi.org/10.1016/j.rse.2019.04.026, 2019.

35 Bindlish, R., Kustas, W. P., French, A. N., Diak, G. R., and Mecikalski, J. R.: Influence of near-surface soil moisture on regional scale heat fluxes: Model results using microwave remote sensing data from SGP97, IEEE Transactions on Geoscience and Remote Sensing, 39, 1719–1728, https://doi.org/10.1109/36.942550, 2001.

Boulet, G., Mougenot, B., Lhomme, J. P., Fanise, P., Lili-Chabaane, Z., Olioso, A., Bahir, M., Rivalland, V., Jarlan, L., Merlin, O., Coudert, B., Er-Raki, S., and Lagouarde, J. P.: The SPARSE model for the prediction of water stress and evapotranspiration components from thermal infra-red data and its evaluation over irrigated and rainfed wheat, Hydrology and Earth System Sciences, 19, 4653–4672, https://doi.org/10.5194/hess-19-4653-2015, 2015.

5 Chanzy, A. and Bruckler, L.: Significance of soil surface moisture with respect to daily bare soil evaporation, Water Resources Research, 29, 1113–1125, https://doi.org/10.1029/92WR02747, http://doi.wiley.com/10.1029/92WR02747, 1993.

Chirouze, J., Boulet, G., Jarlan, L., Fieuzal, R., Rodriguez, J. C., Ezzahar, J., Bigeard, G., and Merlin, O.: Intercomparison of four remote-sensing-based energy balance methods to retrieve surface evapotranspiration and water stress of irrigated fields in semi-arid climate, Hydrology and Earth System Sciences, 18, 1165–1188, https://doi.org/10.5194/hess-18-1165-2014, 2014.

10 Colaizzi, P. D., Kustas, W. P., Anderson, M. C., Agam, N., Tolk, J. A., Evett, S. R., Howell, T. A., Gowda, P. H., and O'shaughnessy, S. A.: Two-source energy balance model estimates of evapotranspiration using component and composite surface temperatures q, Advances in Water Resources, 50, 134–151, https://doi.org/10.1016/j.advwatres.2012.06.004, http://dx.doi.org/10.1016/j.advwatres.2012.06.004, 2012.

Cosby, B. J., Hornberger, G. M., Clapp, R. B., and Ginn, T. R.: A Statistical Exploration of the Relationships of Soil Moisture Char-
15 acteristics to the Physical Properties of Soils, Tech. Rep. 6, http://denning.atmos.colostate.edu/readings/Land/Water{_}Resour.{_}Res.{_}1984{_}Cosby.pdf, 1984.

Entekhabi, D., Njoku, E. G., O'Neill, P. E., Kellogg, K. H., Crow, W. T., Edelstein, W. N., Entin, J. K., Goodman, S. D., Jackson, T. J., Johnson, J., Kimball, J., Piepmeier, J. R., Koster, R. D., Martin, N., McDonald, K. C., Moghaddam, M., Moran, S., Reichle, R., Shi, J. C., Spencer, M. W., Thurman, S. W., Tsang, L., and Van Zyl, J.: The Soil Moisture Active Passive {(SMAP)} Mission, Proc. IEEE, 98,
20 704–716, https://doi.org/10.1117/12.795910, 2010.

Er-Raki, S., Chehbouni, A., Guemouria, N., Duchemin, B., Ezzahar, J., and Hadria, R.: Combining FAO-56 model and ground-based remote sensing to estimate water consumptions of wheat crops in a semi-arid region, Agricultural Water Management, 87, 41–54, https://doi.org/10.1016/j.agwat.2006.02.004, http://linkinghub.elsevier.com/retrieve/pii/S037837740600045X, 2007.

Escorihuela, M., Chanzy, A., Wigneron, J., and Kerr, Y.: Effective soil moisture sampling depth of L-band radiometry: A case study, Remote
25 Sensing of Environment, 114, 995–1001, https://doi.org/10.1016/J.RSE.2009.12.011, https://www.sciencedirect.com/science/article/pii/S0034425709003678, 2010.

Fisher, J. B., Tu, K. P., and Baldocchi, D. D.: Global estimates of the land-atmosphere water flux based on monthly AVHRR and ISLSCP-II data, validated at 16 FLUXNET sites, Remote Sensing of Environment, 112, 901–919, https://doi.org/10.1016/j.rse.2007.06.025, www.elsevier.com/locate/rse, 2008.

30 Fisher, J. B., Melton, F., Middleton, E., Hain, C., Anderson, M., Allen, R., Mccabe, M. F., Hook, S., Baldocchi, D., Townsend, P. A., Kilic, A., Tu, K., Miralles, D. D., Perret, J., Lagouarde, J.-P., Waliser, D., Purdy, A. J., French, A., Schimel, D., Famiglietti, J. S., Stephens, G., and Wood, E. F.: The future of evapotranspiration: Global requirements for ecosystem functioning, carbon and climate feedbacks, agricultural management, and water resources, Water Resources Research, 53,, 2618–2626, https://doi.org/10.1002/2016WR020175, https://agupubs.onlinelibrary.wiley.com/doi/pdf/10.1002/2016WR020175{%}4010.1002/{%}28ISSN{%}291944-9208.COMHES1, 2017.

35 Gan, G. and Gao, Y.: Estimating time series of land surface energy fluxes using optimized two source energy balance schemes : Model formulation , calibration , and validation, Agricultural and Forest Meteorology, 208, 62–75, https://doi.org/10.1016/j.agrformet.2015.04.007, http://dx.doi.org/10.1016/j.agrformet.2015.04.007, 2015.

Gentine, P., Entekhabi, D., Polcher, J., Gentine, P., Entekhabi, D., and Polcher, J.: The Diurnal Behavior of Evaporative Fraction in the Soil–Vegetation–Atmospheric Boundary Layer Continuum, Journal of Hydrometeorology, 12, 1530–1546, https://doi.org/10.1175/2011JHM1261.1, http://journals.ametsoc.org/doi/abs/10.1175/2011JHM1261.1, 2011.

Gerhards, M., Schlerf, M., Mallick, K., and Udelhoven, T.: Challenges and future perspectives of multi-/Hyperspectral thermal infrared remote sensing for crop water-stress detection: A review, Remote Sensing, 11, https://doi.org/10.3390/rs11101240, 2019.

Gokmen, M., Vekerdy, Z., Verhoef, A., Verhoef, W., Batelaan, O., and Tol, C. V. D.: Remote Sensing of Environment Integration of soil moisture in SEBS for improving evapotranspiration estimation under water stress conditions, Remote Sensing of Environment, 121, 261–274, https://doi.org/10.1016/j.rse.2012.02.003, http://dx.doi.org/10.1016/j.rse.2012.02.003, 2012.

Gonzalez-dugo, M. P., Neale, C. M. U., Mateos, L., Kustas, W. P., Prueger, J. H., Anderson, M. C., and Li, F.: Agricultural and Forest Meteorology A comparison of operational remote sensing-based models for estimating crop evapotranspiration, Agricultural and Forest Meteorology, 149, 1843–1853, https://doi.org/10.1016/j.agrformet.2009.06.012, 2009.

Jarlan, L., Khabba, S., Er-Raki, S., Le Page, M., Hanich, L., Fakir, Y., Merlin, O., Mangiarotti, S., Gascoin, S., Ezzahar, J., Kharrou, M. H., Berjamy, B., Saaïdi, A., Boudhar, A., Benkaddour, A., Laftouhi, N., Abaoui, J., Tavernier, A., Boulet, G., Simonneaux, V., Driouech, F., El Adnani, M., El Fazziki, A., Amenzou, N., Raibi, F., El Mandour, A., Ibouh, H., Le Dantec, V., Habets, F., Tramblay, Y., Mougenot, B., Leblanc, M., El Faïz, M., Drapeau, L., Coudert, B., Hagolle, O., Filali, N., Belaqziz, S., Marchane, A., Szczypta, C., Toumi, J., Diarra, A., Aouade, G., Hajhouji, Y., Nassah, H., Bigeard, G., Chirouze, J., Boukhari, K., Abourida, A., Richard, B., Fanise, P., Kasbani, M., Chakir, A., Zribi, M., Marah, H., Naimi, A., Mokssit, A., Kerr, Y., and Escadafal, R.: Remote Sensing of Water Resources in Semi-Arid Mediterranean Areas: the joint international laboratory TREMA, International Journal of Remote Sensing, 36, 4879–4917, https://doi.org/10.1080/01431161.2015.1093198, https://doi.org/10.1080/01431161.2015.1093198, 2015.

Jin, Y., Randerson, J. T., and Goulden, M. L.: Continental-scale net radiation and evapotranspiration estimated using MODIS satellite observations, Remote Sensing of Environment, 115, 2302–2319, https://doi.org/10.1016/j.rse.2011.04.031, http://dx.doi.org/10.1016/j.rse.2011.04.031, 2011.

Kerr, Y. H., Waldteufel, P., Wigneron, J.-P., Delwart, S., Cabot, F., Boutin, J., Escorihuela, M.-J., Font, J., Reul, N., Gruhier, C., Juglea, S. E., Drinkwater, M. R., Hahne, A., Martín-Neira, M., Mecklenburg, S., Kerr, Y. H., Cabot, F., Gruhier, C., Juglea, S. E., Wigneron, J.-P., Delwart, S., Drinkwater, M. R., Hahne, A., and Martín, M.: The SMOS Mission: New Tool for Monitoring Key Elements of the Global Water Cycle, Proceedings of the IEEE |, 98, https://doi.org/10.1109/JPROC.2010.2043032, https://archimer.ifremer.fr/doc/00004/11483/8065.pdf, 2010.

Kerr, Y. H., Member, S., Waldteufel, P., Richaume, P., Pierre Wigneron, J., Ferrazzoli, P., Mahmoodi, A., Al Bitar, A., Cabot, F., Gruhier, C., Enache Juglea, S., Leroux, D., Mialon, A., Delwart, S., Kerr, Y. H., Richaume, P., Al Bitar, A., Cabot, F., Gruhier, C., Juglea, S. E., Leroux, D., Mialon, A., and Wigneron, J. P.: The SMOS Soil Moisture Retrieval Algorithm, IEEE TRANSACTIONS ON GEOSCIENCE AND REMOTE SENSING, 50, https://doi.org/10.1109/TGRS.2012.2184548, http://ieeexplore.ieee.org., 2012.

Kharrou, M. H., Er-Raki, S., Chehbouni, A., Duchemin, B., Simonneaux, V., Lepage, M., Ouzine, L., and Jarlan, L.: Water use efficiency and yield of winter wheat under different irrigation regimes in a semi-arid region, Agricultural Sciences, 2, 273–282, https://doi.org/10.4236/as.2011.23036, http://www.scirp.org/journal/AS/, 2011.

Kustas, W. and Norman, J.: Evaluation of soil and vegetation heat flux predictions using a simple two-source model with radiometric temperatures for partial canopy cover, Agricultural and Forest Meteorology, 94, 13–29, https://doi.org/10.1016/S0168-1923(99)00005-2, 1999.

Kustas, W. and Norman, J. M.: A two-source approach for estimating turbulent fluxes using multiple angle thermal infrared observations, Water Resources Research, 33, 1495–1508, https://doi.org/10.1029/97WR00704, http://doi.wiley.com/10.1029/97WR00704, 1997.

Kustas, W., Zhan, X., and Jackson, T.: Mapping surface energy flux partitioning at large scales with optical and microwave remote sensing data from Washita '92, Tech. Rep. 1, https://doi.org/10.1029/98WR02094, http://hydrolab.arsusda.gov/washita92/, 1999.

5 Kustas, W. P., Zhan, X., and Schmugge, T. J.: Combining optical and microwave remote sensing for mapping energy fluxes in a semiarid watershed, Remote Sensing of Environment, 64, 116–131, https://doi.org/10.1016/S0034-4257(97)00176-4, 1998.

Lewis, P. and Barnsley, M. J.: Influence of the sky radiance distribution on various formulations of the earth surface albedo, Remote Sensing Unit, pp. 707–715, http://www2.geog.ucl.ac.uk/{~}plewis/LewisBarnsley1994.pdf, 1994.

Lhomme, J.-P. and Elguero, E.: Examination of evaporative fraction diurnal behaviour using a soil-vegetation model coupled with
10 a mixed-layer model, Hydrology and Earth System Sciences, 3, 259–270, https://doi.org/10.5194/hess-3-259-1999, http://www.hydrol-earth-syst-sci.net/3/259/1999/, 1999.

Li, F., Kustas, W. P., Anderson, M. C., Jackson, T. J., Bindlish, R., and Prueger, J. H.: Comparing the utility of microwave and thermal remote-sensing constraints in two-source energy balance modeling over an agricultural landscape, Remote Sensing of Environment, 101, 315–328, https://doi.org/10.1016/j.rse.2006.01.001, 2006.

15 Littell, J. S., Peterson, D. L., Riley, K. L., Liu, Y., and Luce, C. H.: A review of the relationships between drought and forest fire in the United States, Global Change Biology, 22, 2353–2369, https://doi.org/10.1111/gcb.13275, http://doi.wiley.com/10.1111/gcb.13275, 2016.

Long, D. and Singh, V. P.: A Two-source Trapezoid Model for Evapotranspiration (TTME) from satellite imagery, Remote Sensing of Environment, 121, 370–388, https://doi.org/10.1016/j.rse.2012.02.015, http://dx.doi.org/10.1016/j.rse.2012.02.015, 2012.

Malbéteau, Y., Merlin, O., Molero, B., Rüdiger, C., and Bacon, S.: DisPATCh as a tool to evaluate coarse-scale remotely sensed soil moisture
20 using localized in situ measurements: Application to SMOS and AMSR-E data in Southeastern Australia, International Journal of Applied Earth Observation and Geoinformation, 45, 221–234, https://doi.org/10.1016/j.jag.2015.10.002, http://linkinghub.elsevier.com/retrieve/pii/S0303243415300386, 2016.

Malbéteau, Y., Merlin, O., Balsamo, G., Er-Raki, S., Khabba, S., Walker, J. P., Jarlan, L., Malbéteau, Y., Merlin, O., Balsamo, G., Er-Raki, S., Khabba, S., Walker, J. P., and Jarlan, L.: Toward a Surface Soil Moisture Product at High Spatiotemporal Resolution: Temporally In-
25 terpolated, Spatially Disaggregated SMOS Data, Journal of Hydrometeorology, 19, 183–200, https://doi.org/10.1175/JHM-D-16-0280.1, http://journals.ametsoc.org/doi/10.1175/JHM-D-16-0280.1, 2018.

Mallick, K., Jarvis, A. J., Boegh, E., Fisher, J. B., Drewry, D. T., Tu, K. P., Hook, S. J., Hulley, G., Ardö, J., Beringer, J., Arain, A., and Niyogi, D.: A Surface Temperature Initiated Closure (STIC) for surface energy balance fluxes, Remote Sensing of Environment, 141, 243–261, https://doi.org/10.1016/j.rse.2013.10.022, http://dx.doi.org/10.1016/j.rse.2013.10.022, 2014.

30 Mallick, K., Boegh, E., Trebs, I., Alfieri, J. G., Kustas, W. P., Prueger, J. H., Niyogi, D., Das, N., Drewry, D. T., Hoffmann, L., and Jarvis, A. J.: Penman-Monteith formulation, Water Resources Research, 51, 6214–6243, https://doi.org/10.1002/2014WR016106.Received, 2015.

Mallick, K., Trebs, I., Boegh, E., Giustarini, L., Schlerf, M., Drewry, D. T., Hoffmann, L., Von Randow, C., Kruijt, B., Araùjo, A., Saleska, S., Ehleringer, J. R., Domingues, T. F., Ometto, J. P. H., Nobre, A. D., Luiz Leal De Moraes, O., Hayek, M., William Munger, J., and Wofsy, S. C.: Canopy-scale biophysical controls of transpiration and evaporation in the Amazon Basin, Hydrology and Earth System Sciences,
35 20, 4237–4264, https://doi.org/10.5194/hess-20-4237-2016, 2016.

Merlin, O., Al Bitar, A., Rivalland, V., Béziat, P., Ceschia, E., and Dedieu, G.: An analytical model of evaporation efficiency for unsaturated soil surfaces with an arbitrary thickness, Journal of Applied Meteorology and Climatology, 50, 457–471, https://doi.org/10.1175/2010JAMC2418.1, 2011.

Merlin, O., Rüdiger, C., Al Bitar, A., Richaume, P., Walker, J. P., and Kerr, Y. H.: Disaggregation of SMOS soil moisture in Southeastern Australia, IEEE Transactions on Geoscience and Remote Sensing, 50, 1556–1571, https://doi.org/10.1109/TGRS.2011.2175000, 2012.

Merlin, O., Escorihuela, M. J., Mayoral, M. A., Hagolle, O., Al Bitar, A., and Kerr, Y.: Self-calibrated evaporation-based disaggregation of SMOS soil moisture: An evaluation study at 3km and 100m resolution in Catalunya, Spain, Remote Sensing of Environment, 130, 25–38, https://doi.org/10.1016/j.rse.2012.11.008, 2013.

Merlin, O., Stefan, V. G., Amazirh, A., Chanzy, A., Ceschia, E., Tallec, T., Beringer, J., Gentine, P., Er-Raki, S., Bircher, S., and Khabba, S.: Modeling soil evaporation efficiency in a range of soil and atmospheric conditions: A downward approach based on multi-site data, Submitted to Water Resources Research, pp. 3663–3684, https://doi.org/10.1002/2015WR018233.Received, 2016.

Merlin, O., Olivera-Guerra, L., Aït Hssaine, B., Amazirh, A., Rafi, Z., Ezzahar, J., Gentine, P., Khabba, S., Gascoin, S., and Er-Raki, S.: A phenomenological model of soil evaporative efficiency using surface soil moisture and temperature data, Agricultural and Forest Meteorology, 256-257, 501–515, https://doi.org/10.1016/J.AGRFORMET.2018.04.010, https://www.sciencedirect.com/science/article/pii/S0168192318301321, 2018.

Molden, D., Oweis, T., Steduto, P., Bindraban, P., Hanjra, M. A., and Kijne, J.: Improving agricultural water productivity: Between optimism and caution, Agricultural Water Management, 97, 528–535, https://doi.org/10.1016/J.AGWAT.2009.03.023, https://www.sciencedirect.com/science/article/pii/S0378377409000912, 2010.

Molero, B., Merlin, O., Malbéteau, Y., Al Bitar, A., Cabot, F., Stefan, V., Kerr, Y., Bacon, S., Cosh, M., Bindlish, R., and Jackson, T.: SMOS disaggregated soil moisture product at 1 km resolution: Processor overview and first validation results, Remote Sensing of Environment, 180, 361–376, https://doi.org/10.1016/J.RSE.2016.02.045, https://www.sciencedirect.com/science/article/pii/S0034425716300736, 2016.

Moran, M. S., Clarke, T. R., Inoue, Y., and Vidal, A.: Estimating Crop Water Deficit Using the Relation between Surface-Air Temperature and Spectral Vegetation Index, Remote Sensing of Environment, 49, 246–263, https://naldc.nal.usda.gov/download/146/PDF, 1994.

Morillas, L., Villagarcía, L., Domingo, F., Nieto, H., Uclés, O., and García, M.: Environmental factors affecting the accuracy of surface fluxes from a two-source model in Mediterranean drylands: Upscaling instantaneous to daytime estimates, Agricultural and Forest Meteorology, 189-190, 140–158, https://doi.org/10.1016/j.agrformet.2014.01.018, http://dx.doi.org/10.1016/j.agrformet.2014.01.018, 2014.

Njoku, E. G., Jackson, T. J., Lakshmi, V., Member, S., Chan, T. K., and Nghiem, S. V.: Soil Moisture Retrieval From AMSR-E, IEEE TRANSACTIONS ON GEOSCIENCE AND REMOTE SENSING, 41, https://doi.org/10.1109/TGRS.2002.808243, https://pdfs.semanticscholar.org/4894/bdd44f8daa86c6018879a657b8883b25e375.pdf, 2003.

Norman, J. M., Kustas, W. P., and Humes, K. S.: Source approach for estimating soil and vegetation energy fluxes in observations of directional radiometric surface temperature, Agricultural and Forest Meteorology, 77, 263–293, https://doi.org/10.1016/0168-1923(95)02265-Y, 1995.

Olivera-Guerra, L., Merlin, O., Er-Raki, S., Khabba, S., and Escorihuela, M. J.: Estimating the water budget components of irrigated crops: Combining the FAO-56 dual crop coefficient with surface temperature and vegetation index data, Agricultural Water Management, 208, 120–131, https://doi.org/10.1016/j.agwat.2018.06.014, https://doi.org/10.1016/j.agwat.2018.06.014, 2018.

Owe, M., De Jeu, R., and Holmes, T.: Multisensor historical climatology of satellite-derived global land surface moisture, J. Geophys. Res, 113, 1002, https://doi.org/10.1029/2007JF000769, http://tsdis.gsfc.nasa.gov/, 2008.

Peng, J., Loew, A., Merlin, O., and Verhoest, N. E.: A review of spatial downscaling of satellite remotely sensed soil moisture, Reviews of Geophysics, 55, https://doi.org/10.1002/2016RG000543, 2017.

Priestley, C. H. B. and Taylor, R. J.: On the Assessment of Surface Heat Flux and Evaporation Using Large-Scale Parameters, Monthly Weather Review, 100, 81–92, https://doi.org/10.1175/1520-0493(1972)100<0081:OTAOSH>2.3.CO;2, http://journals.ametsoc.org/doi/abs/10.1175/1520-0493{%}281972{%}29100{%}3C0081{%}3AOTAOSH{%}3E2.3.CO{%}3B2, 1972.

Purdy, A. J., Fisher, J. B., Goulden, M. L., Colliander, A., Halverson, G., Tu, K., and Famiglietti, J. S.: Remote Sensing of Environment SMAP soil moisture improves global evapotranspiration, Remote Sensing of Environment, 219, 1–14, https://doi.org/10.1016/j.rse.2018.09.023, https://doi.org/10.1016/j.rse.2018.09.023, 2018.

Rafi, Z., Merlin, O., Le Dantec, V., Khabba, S., Mordelet, P., Er-Raki, S., Amazirh, A., Olivera-Guerra, L., Ait Hssaine, B., Simonneaux, V., Ezzahar, J., and Ferrer, F.: Partitioning evapotranspiration of a drip-irrigated wheat crop: Intercomparing eddy covariance-, sap flow-, lysimeter- and FAO-based methods, Agricultural and Forest Meteorology, 265, 310–326, https://doi.org/10.1016/J.AGRFORMET.2018.11.031, https://www.sciencedirect.com/science/article/pii/S0168192318303848, 2019.

Roerink, G., Su, Z., and Menenti, M.: S-SEBI: A simple remote sensing algorithm to estimate the surface energy balance, Physics and Chemistry of the Earth, Part B: Hydrology, Oceans and Atmosphere, 25, 147–157, https://doi.org/10.1016/S1464-1909(99)00128-8, https://www.sciencedirect.com/science/article/pii/S1464190999001288, 2000.

Schmid, H. P.: Source areas for scalars and scalar fluxes, Boundary-Layer Meteorology, 67, 293–318, https://doi.org/10.1007/BF00713146, http://link.springer.com/10.1007/BF00713146, 1994.

Sellers, P. J., Heiser, M. D., and Hall, F. G.: Relations between surface conductance and spectral vegetation indexes at intermediate (100m2 to 15km2) length scales, J. Geophysical Research-atmospheres, 97, 19 033–19 059, 1992.

Shuttleworth, W., Gurney, R., Hsu, A., and Ormsby, J.: FIFE: the variation in energy partition at surface flux sites, Remote Sensing and Large-Scale Global Porcesses (IAHS Publ.), 186, 67–74, 1989.

Su, Z.: The Surface Energy Balance System (SEBS) for estimation of turbulent heat fluxes, Hydrology and Earth System Sciences, 6, 85–100, https://doi.org/10.1109/VLSID.2007.18, http://www.hydrol-earth-syst-sci.net/6/85/2002/, 2002.

Twine, T. E., Kustas, W. P., Norman, J. M., Cook, D. R., Houser, P. R., Meyers, T. P., Prueger, J. H., Starks, P. J., Wesley, M. L., and Wesely, M. L.: Correcting eddy-covariance flux underestimates over a grassland, Tech. rep., http://digitalcommons.unl.edu/nasapub/11http://digitalcommons.unl.edu/nasapub/11, 2000.

Wang, Y., Li, X., and Tang, S.: Validation of the SEBS-derived sensible heat for FY3A / VIRR and TERRA / MODIS over an alpine grass region using LAS measurements, International Journal of Applied Earth Observations and Geoinformation, 23, 226–233, https://doi.org/10.1016/j.jag.2012.09.005, http://dx.doi.org/10.1016/j.jag.2012.09.005, 2013.

Yang, Y., Guan, H., Long, D., Liu, B., Qin, G., Qin, J., and Batelaan, O.: Estimation of surface soil moisture from thermal infrared remote sensing using an improved trapezoid method, Remote Sensing, 7, https://doi.org/10.3390/rs70708250, 2015.

Yao, Y., Liang, S., Yu, J., Zhao, S., Lin, Y., Jia, K., Zhang, X., Cheng, J., Xie, X., Sun, L., Wang, X., and Zhang, L.: Differences in estimating terrestrial water flux from three satellite-based Priestley-Taylor algorithms, International Journal of Applied Earth Observation and Geoinformation, 56, 1–12, https://doi.org/10.1016/j.jag.2016.10.009, http://linkinghub.elsevier.com/retrieve/pii/S0303243416301854, 2017.

Yu, W., Ma, M., Li, Z., Tan, J., and Wu, A.: New scheme for validating remote-sensing land surface temperature productswith stationobservations, Remote Sensing, 9, 1–24, https://doi.org/10.3390/rs9121210, 2017.
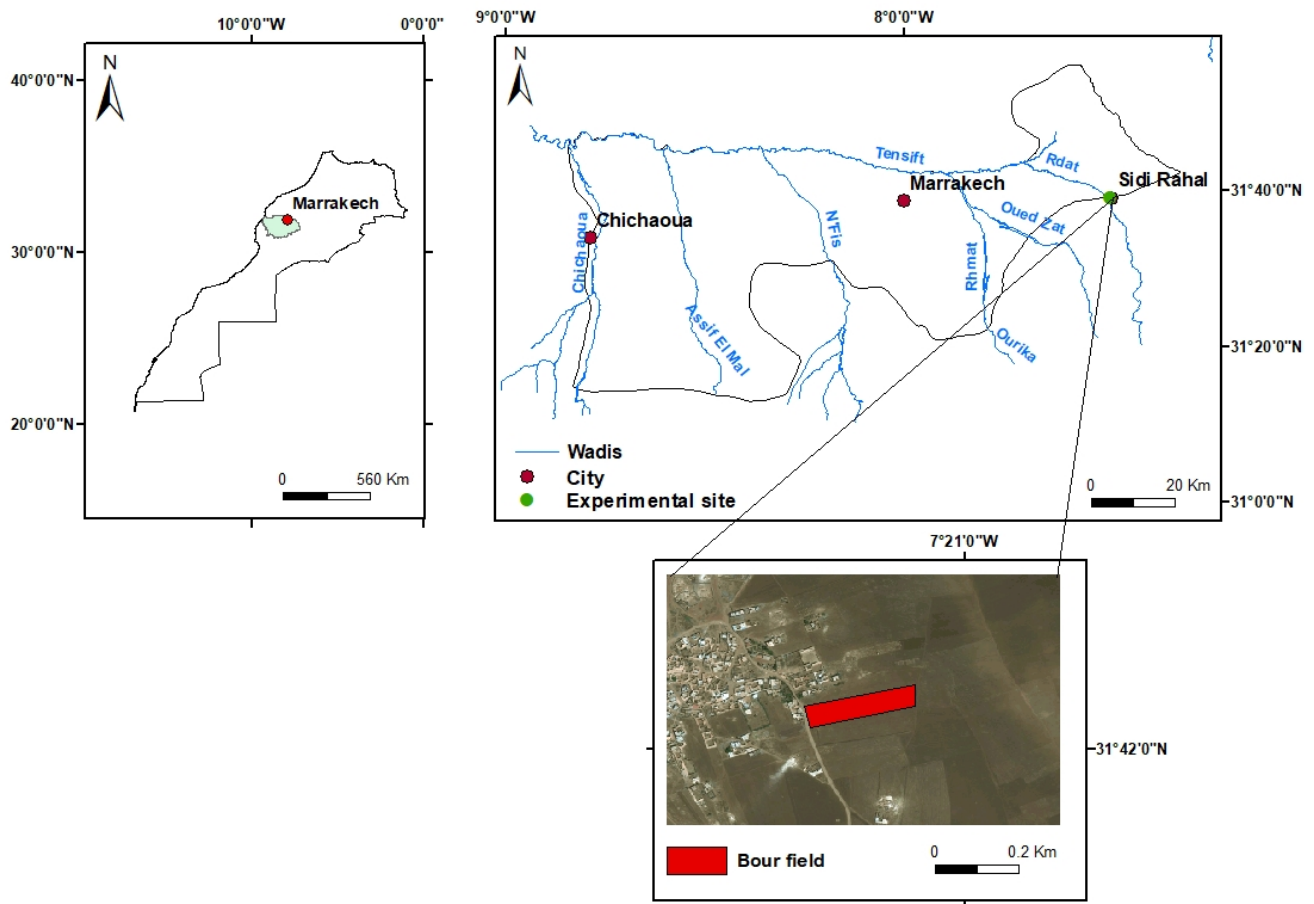
Figure 1. Location of Sidi Rahal site (east of Marrakech) in the Tensift basin, central of Morocco.
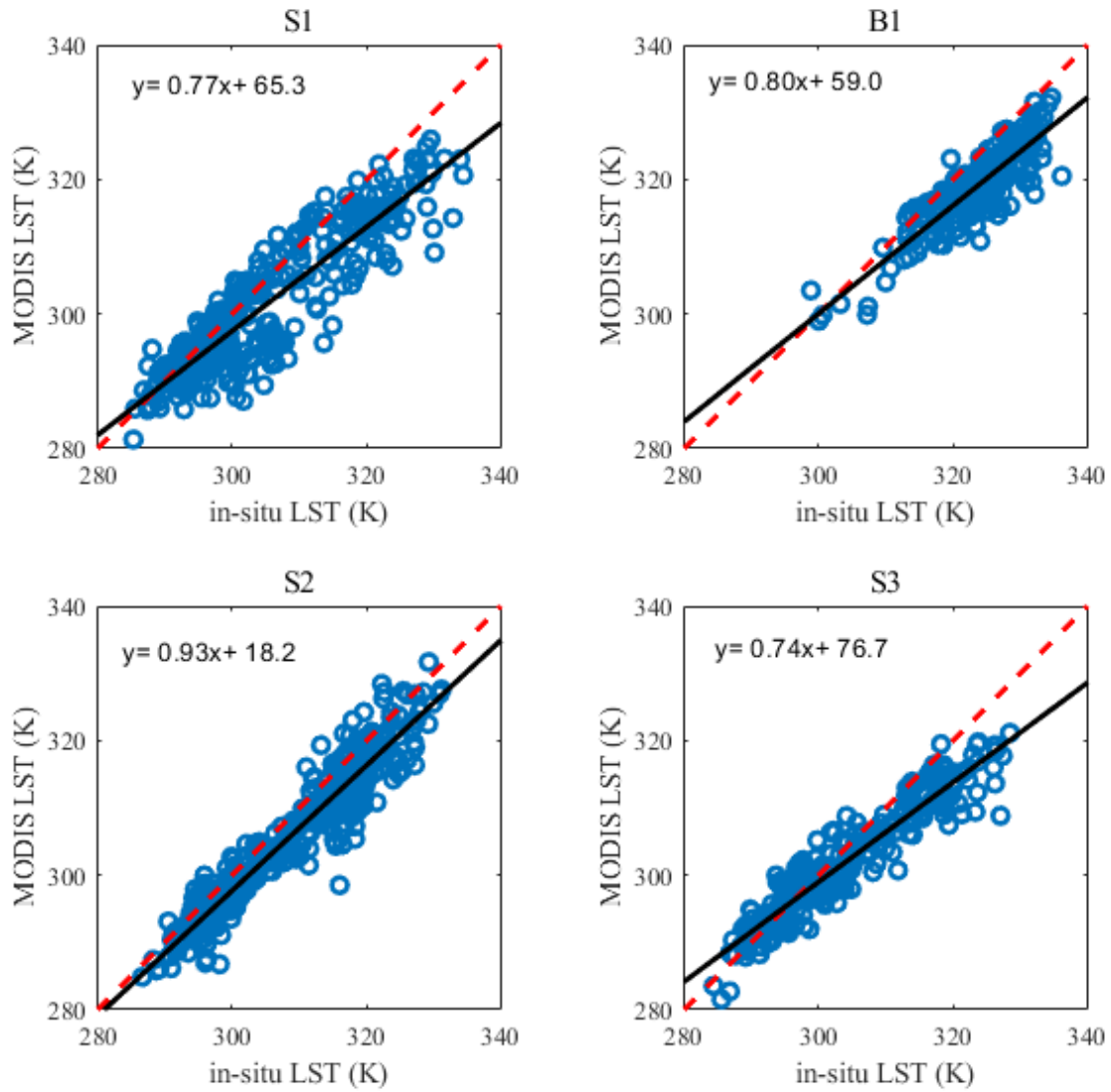
Figure 2. Scatter plots of MODIS versus in-situ *LST* at Sidi Rahal site for S1 (2014-2015), B1 (2015-2016), S2 (2016-2017) and S3 (2017-2018) agricultural seasons, separately, (red dashed line is the line(1:1)-black line is the regression line).
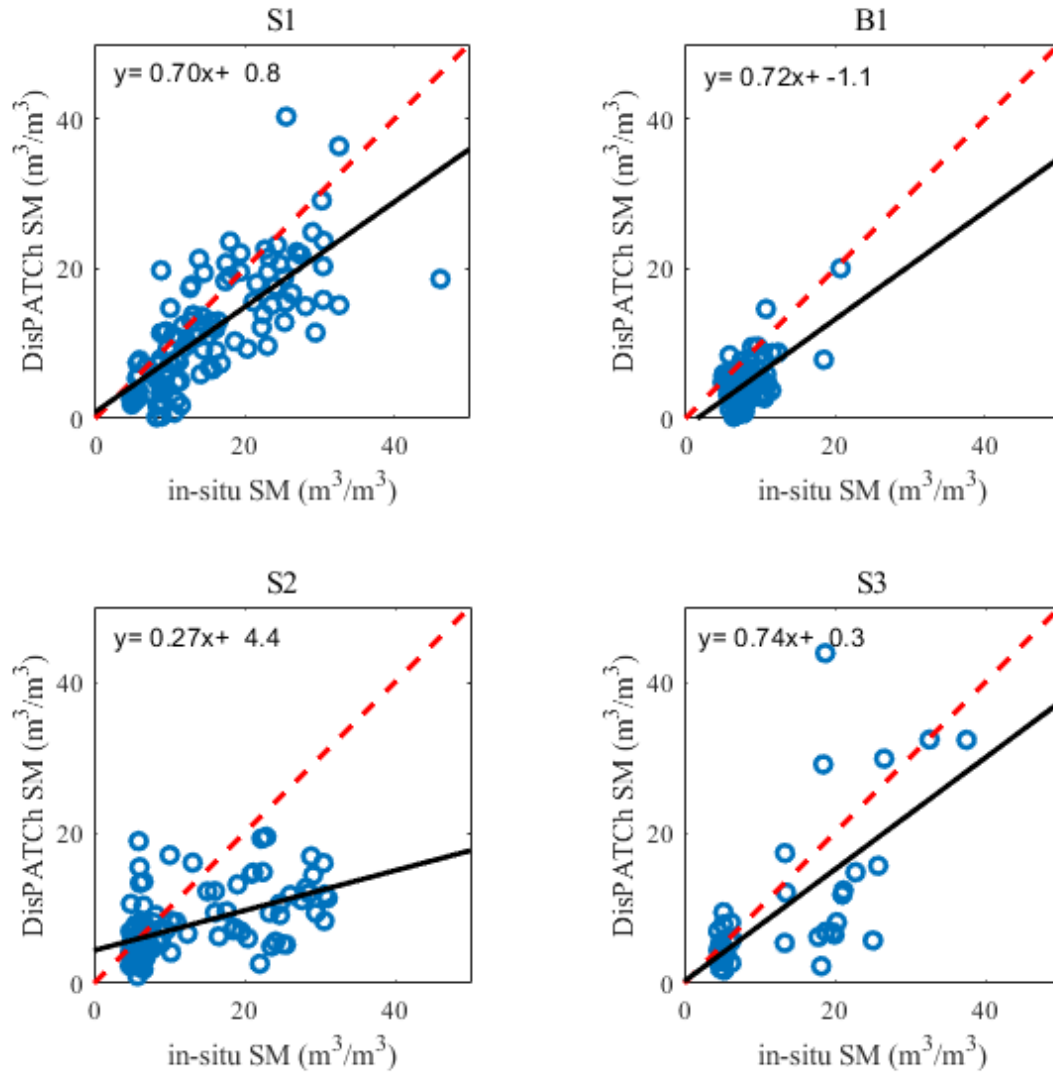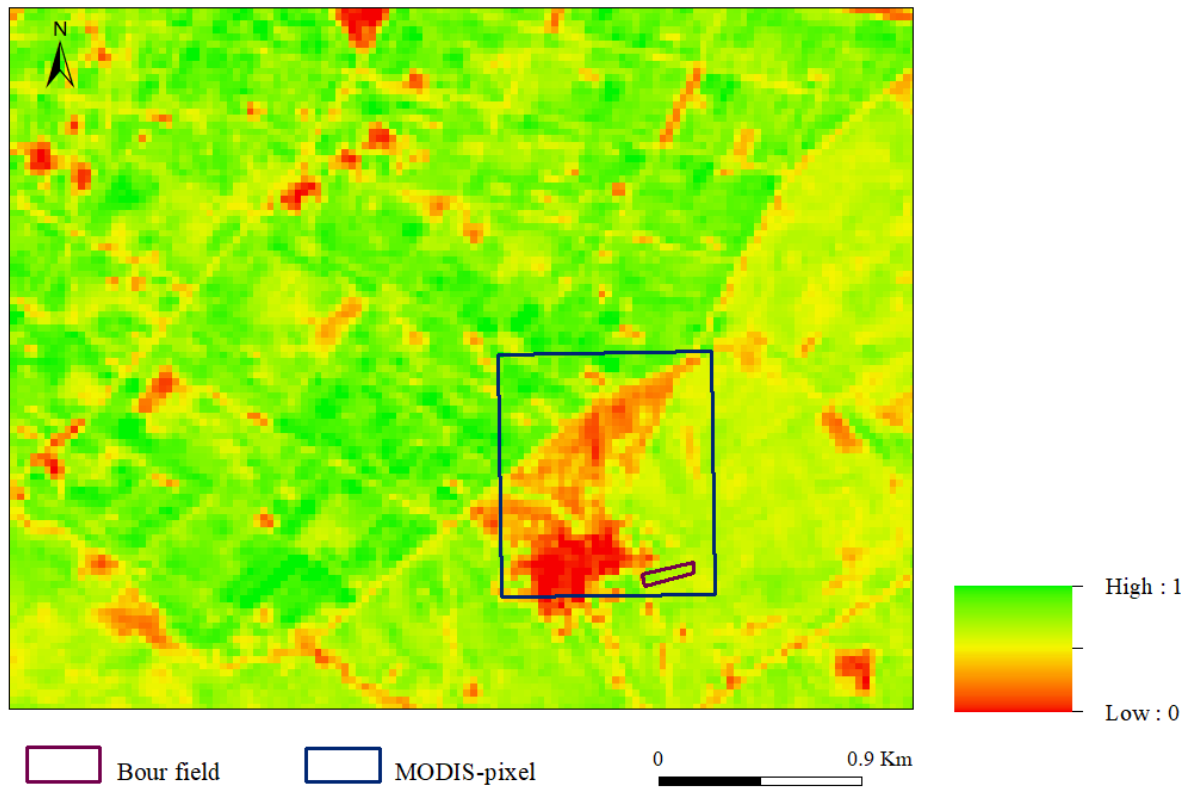
Figure 3. Scatter plots of the 1 km resolution DisPATCh versus in-situ SM at Sidi Rahal site for S1 (2014-2015), B1 (2015-2016), S2 (2016-2017) and S3 (2017-2018) agricultural seasons, separately.

Figure 4. $NDVI$ image derived from Landsat data acquired on 17/04/2018. The experimental field and the overlaying 1 km resolution MODIS pixel are superimposed.
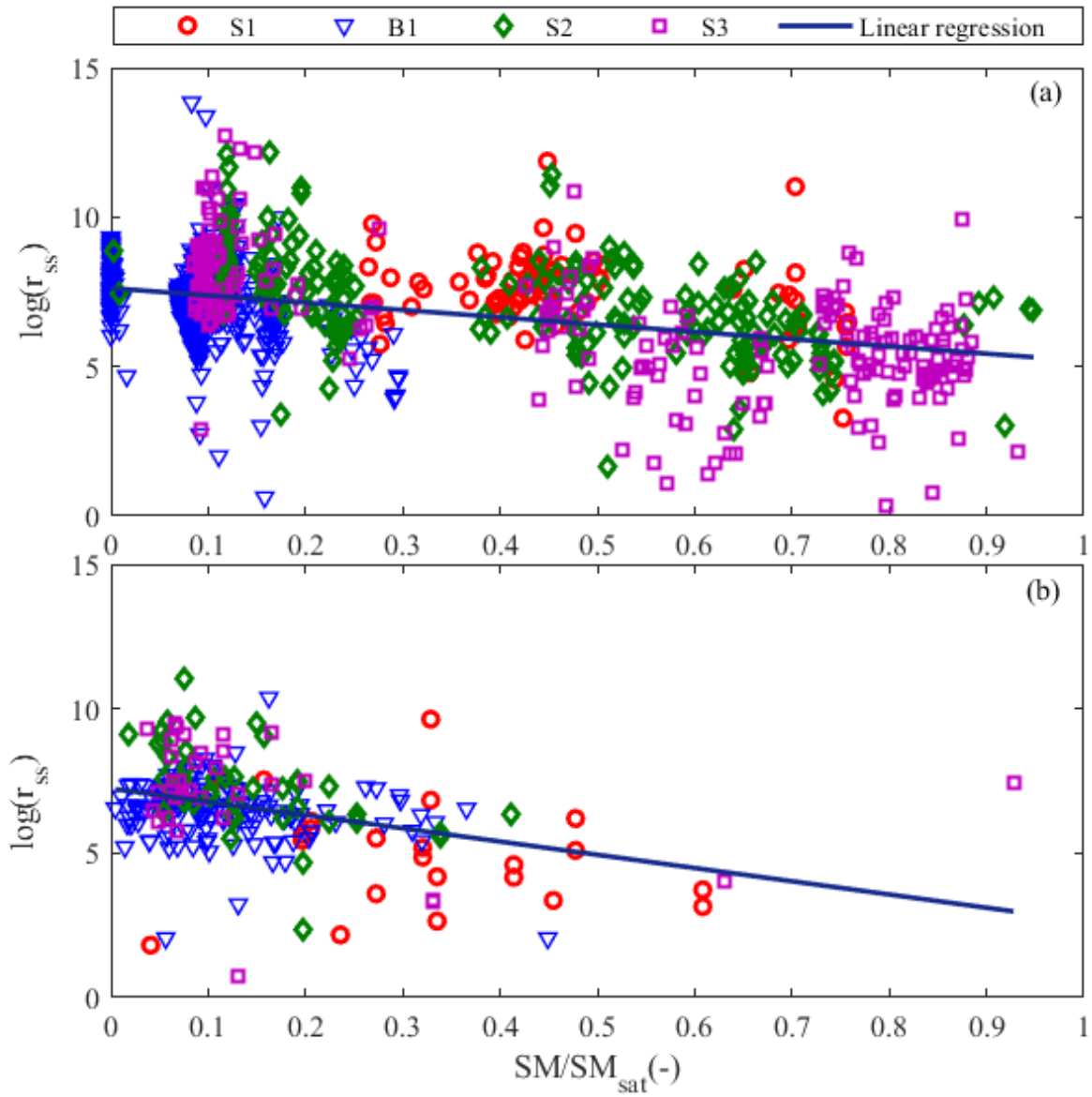
Figure 5. $\log(r_{ss})$ versus SM/SM_{sat} (calibration step 1) using in-situ (a) and satellite (b) data.
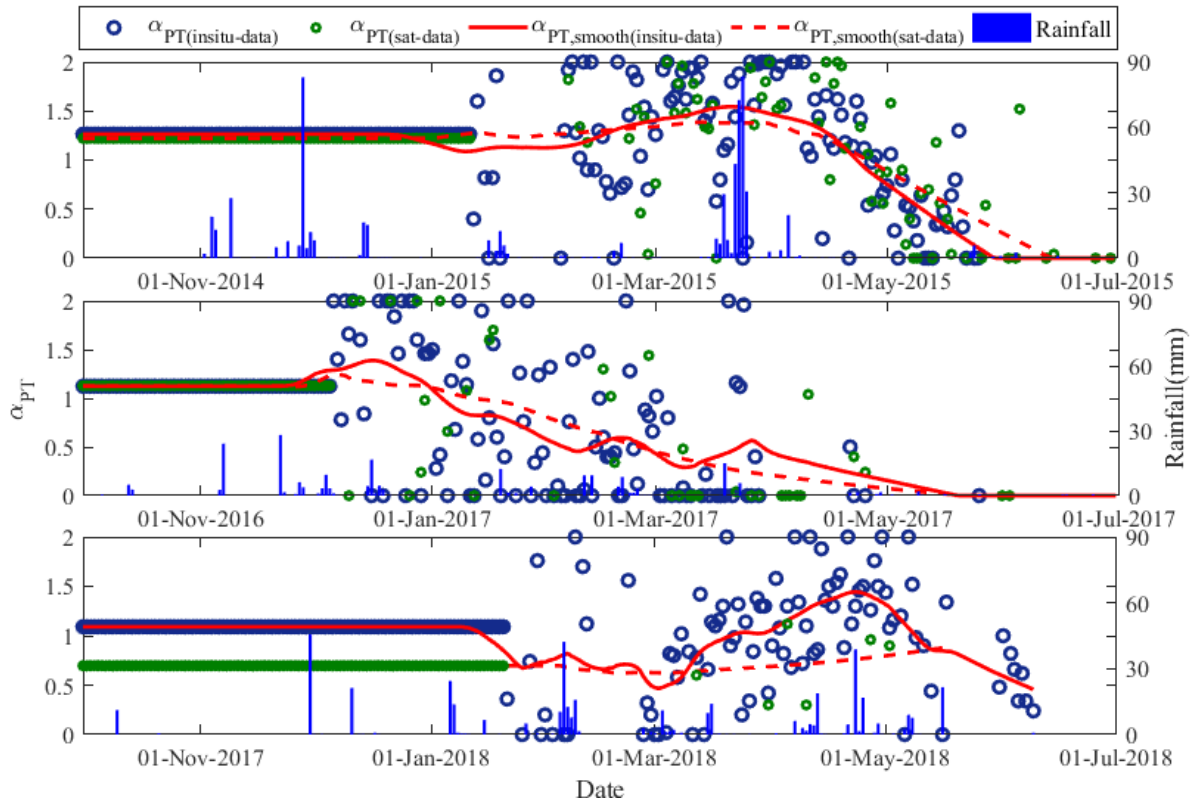
Figure 6. Time series of daily retrieved and smoothed α_{PT} (calibration step 2-using in-situ data, and satellite data) collected during S1, S2 and S3.
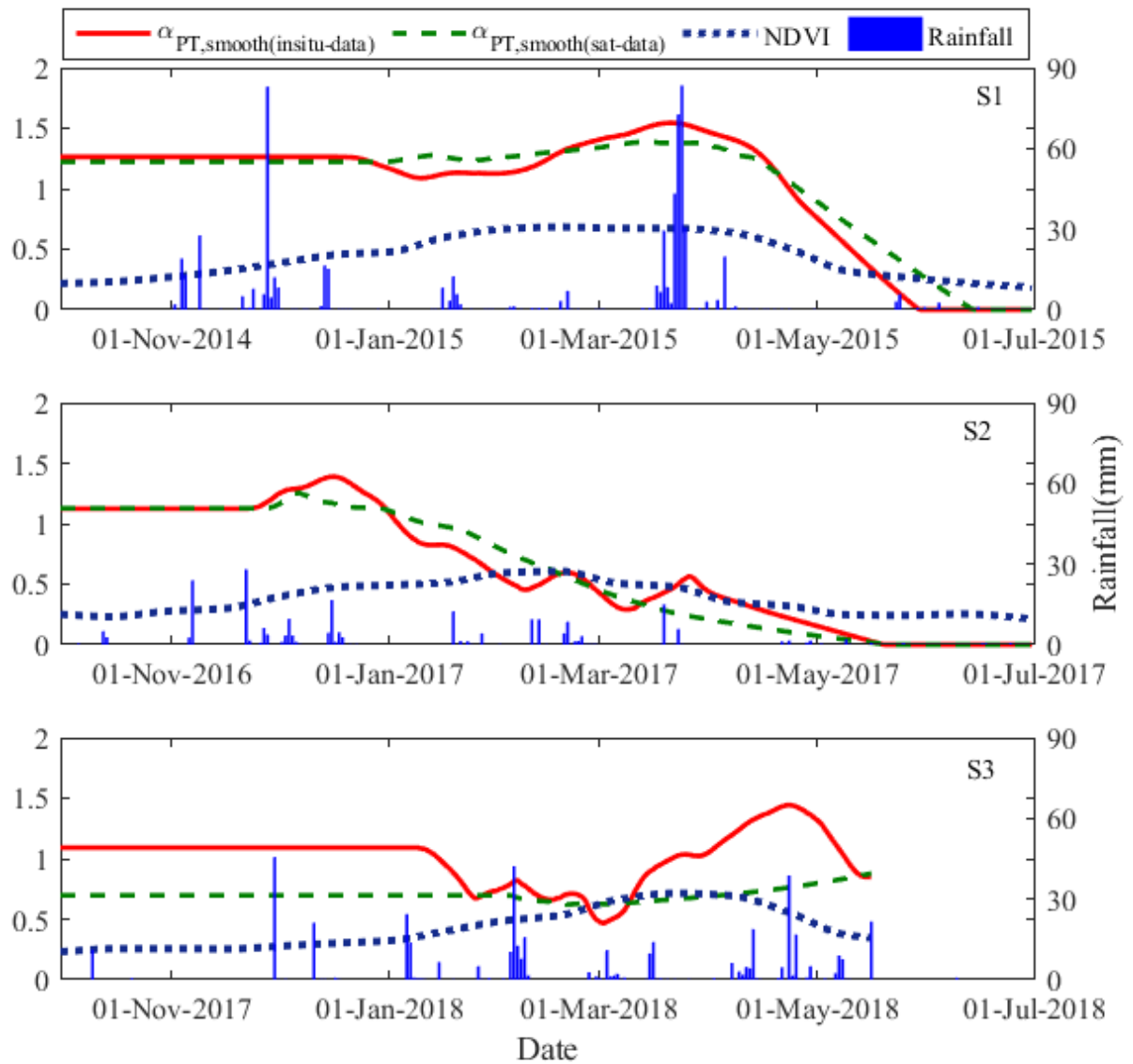
Figure 7. Time series of calibrated daily α_{PT} (red-using in-situ data, green- using satellite data) superimposed with $NDVI$ and the rainfall events during S1, S2 and S3, separately.
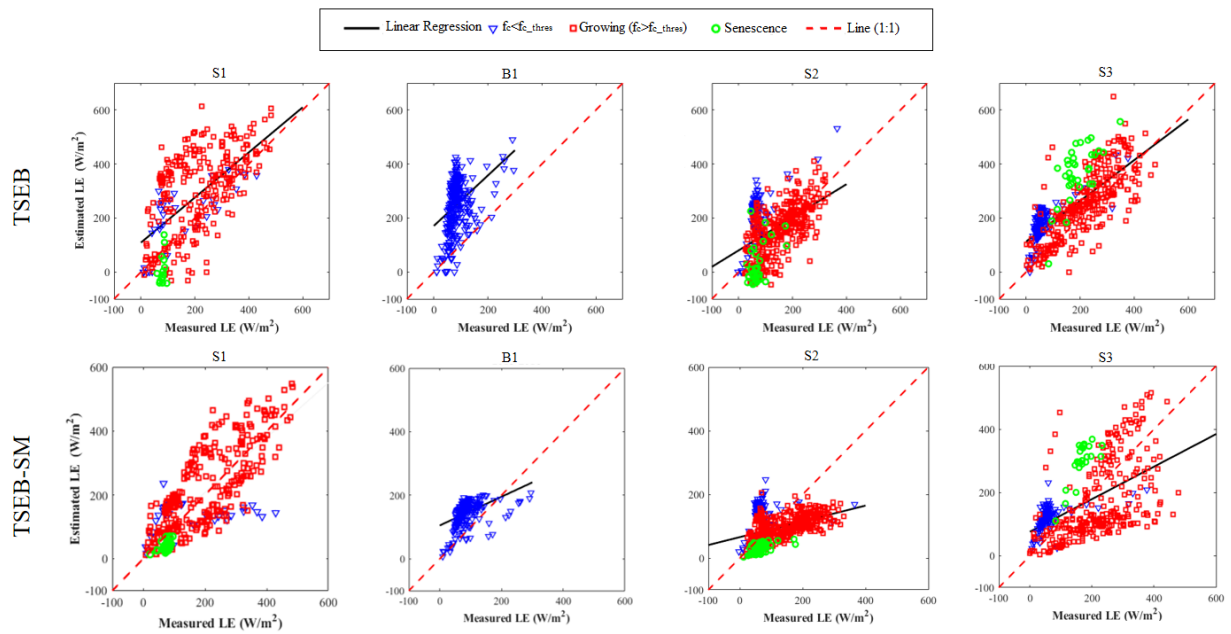
Figure 8. Scatterplot of simulated versus observed LE for (top) TSEB and (bottom) TSEB-SM models using in-situ data collected during S1, B1, S2 and S3, respectively.
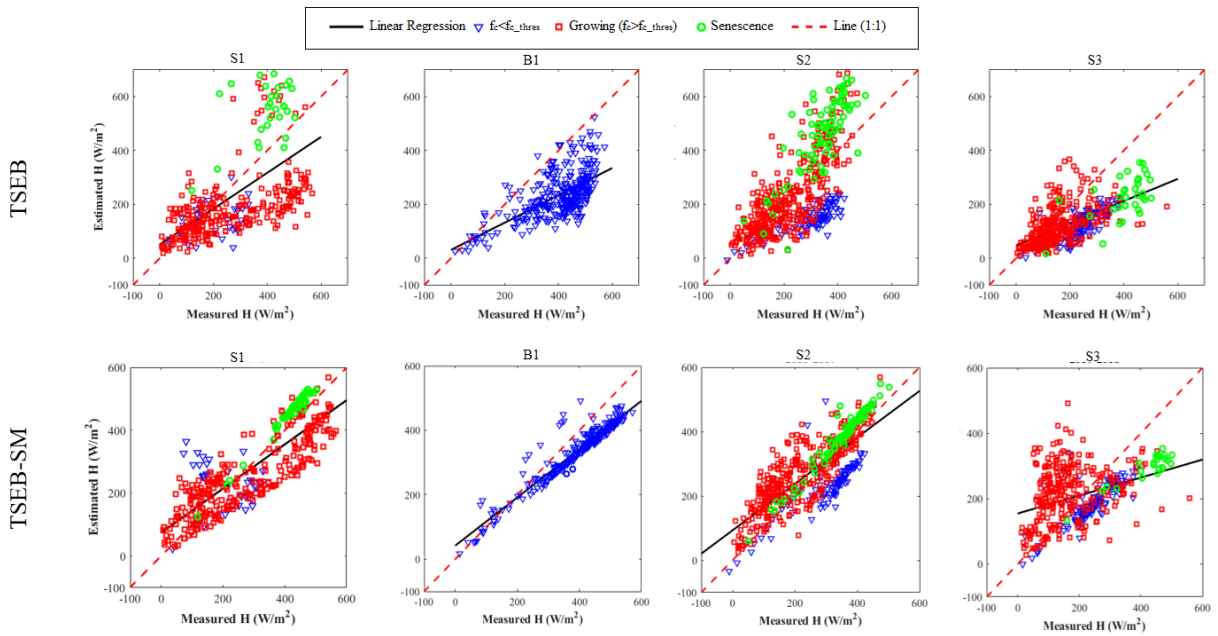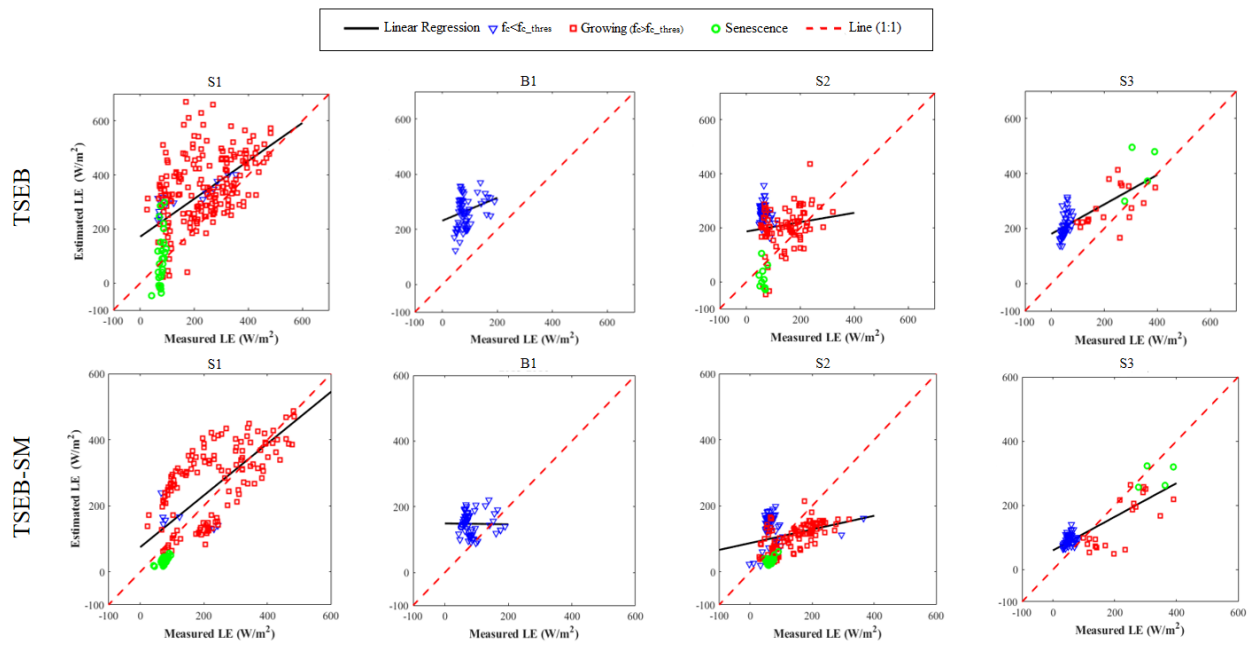
Figure 9. Same as Fig. 8 but for *H* fluxes.
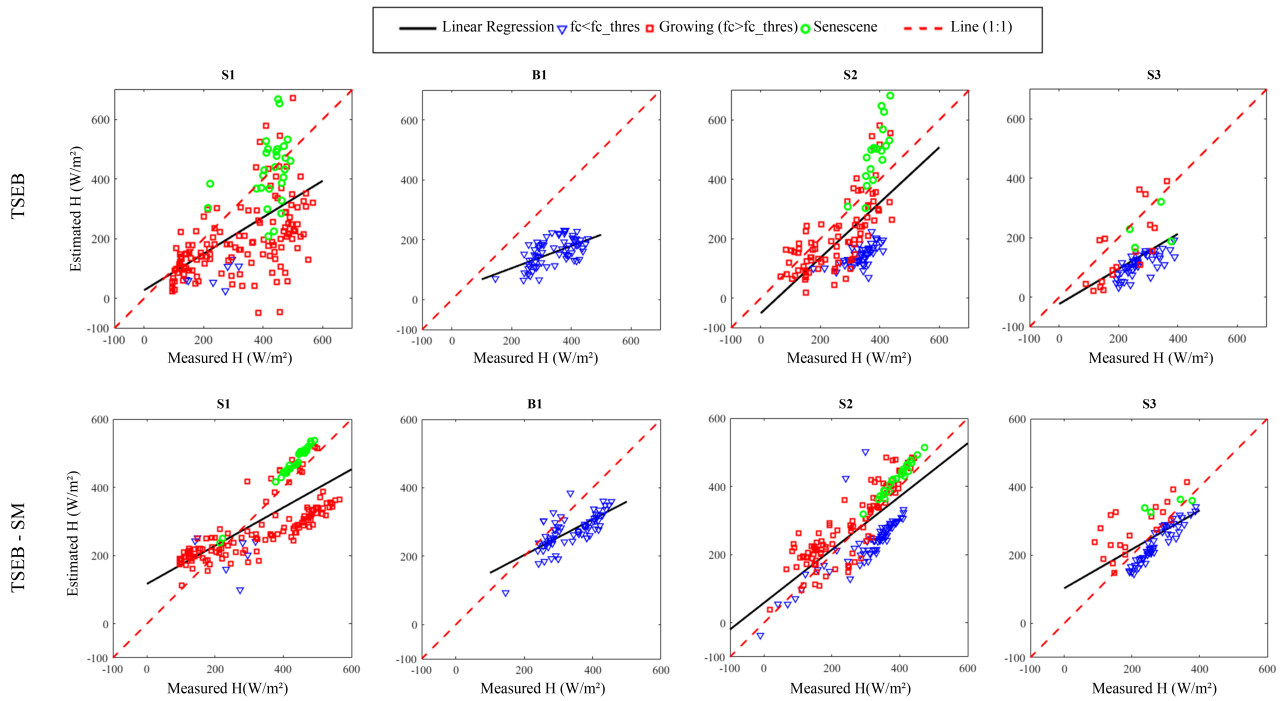
Figure 10. Same as Fig. 8 but for satellite data.

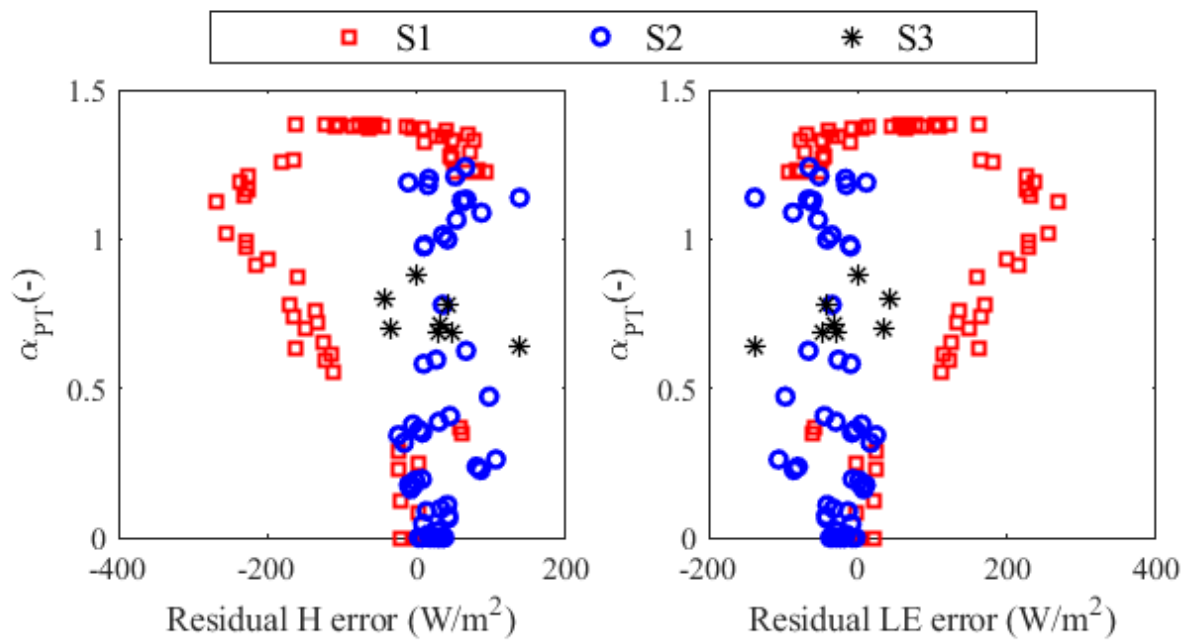**Figure 11.** Same as Fig. 8 but for *H* fluxes and satellite data.

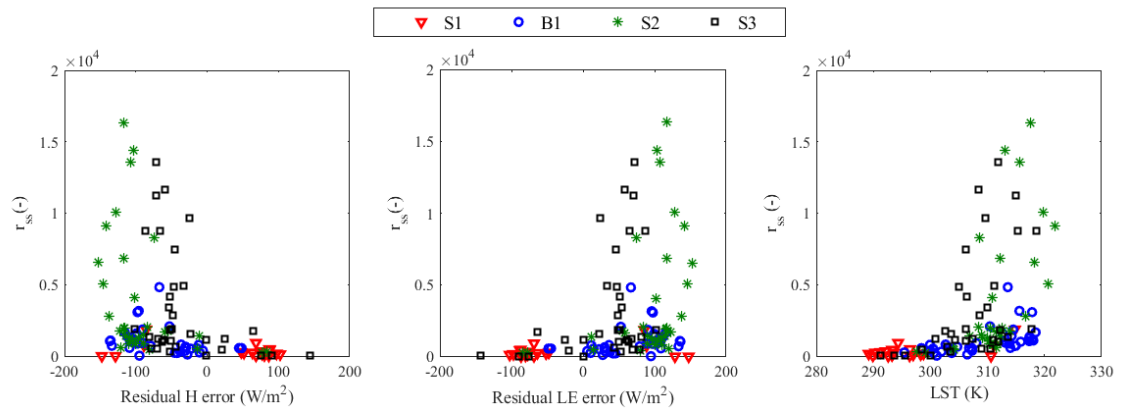**Figure 12.** α_{PT} vs residual H and LE error.

Figure 13. Retrieved r_{ss} vs residual H (left) and LE (middle) error and LST (right) for the four study periods separately.
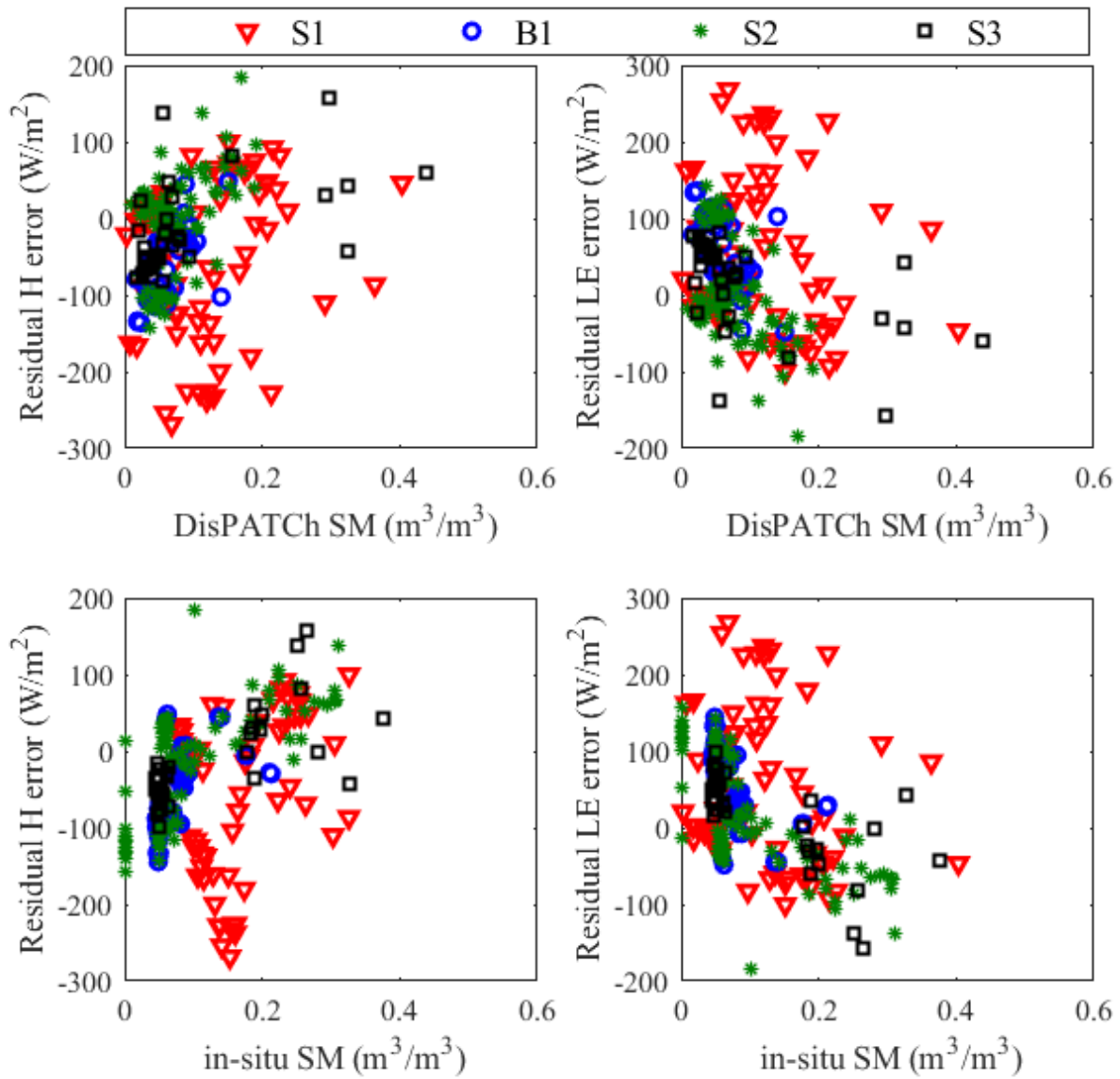
Figure 14. Residual H (left) and LE (right) errors vs DisPATCh (top) and in-situ (bottom) SM.

Table 1. Characteristics of the study site.

Study period	R ainfall amount (mm)	Field status
Oct 2014- Jun 2015 (S1)	608	Cultivated
Aug 2015- Sep 2016 (B1)	157	Bare soil
Sep 2016- Jun 2017 (S2)	214	Cultivated
Oct 2017- Jun 2018 (S3)	481	Cultivated

Table 2. Mean equations of TSEB-SM.

Variable	Equation	Value range
Soil heat flux	$LE_{soil} = \dfrac{\rho c_p}{\gamma} \dfrac{e_s - e_a}{r_{ah} + r_s + r_{ss}}$	0-600 W/m^2
Resistance to vapor diffusion in the soil	$r_{ss} = \exp(a_{rss} - b_{rss} \times \dfrac{SM}{SM_{sat}}$	a_{rss} and b_{rss} : (1-13)
Soil moisture at saturation	$SM_{sat} = 0.1 \times (-108 \times f_{sand} + 49.305)$	0.47m^3/m^3
Cost function for minimizing r_{ss}	$F_{inst} = (T_{surf,sim} - T_{surf,mes})$	F_{inst} = 5 K
Vegetation latent heat flux	$\alpha_{PT}.f_g.\dfrac{\triangle}{\triangle + \gamma}.R_{n,veg}$	α_{PT} (0-2) f_g =1

Table 3. Validation results of DisPATCh SM and MODIS LST at Sidi Rahal site.

	Period	R^2	$RMSE$	MBE
LST	S1	0.8	6.4 (K)	-3.7 (K)
	B1	0.76	5.6 (K)	-4.6(K)
	S2	0.91	4.3 (K)	-2.9 (K)
	S3	0.89	4 (K)	-2 (K)
SM	S1	0.55	$0.07\ m^3/m^3$	$-0.04\ m^3/m^3$
	B1	0.36	$0.04\ m^3/m^3$	$-0.03\ m^3/m^3$
	S2	0.27	$0.09\ m^3/m^3$	$-0.05\ m^3/m^3$
	S3	0.47	$0.08\ m^3/m^3$	$-0.03\ m^3/m^3$

Table 4. Statistical results ($RMSE$, R^2 and MBE) between modeled and measured sensible and latent heat fluxes for S1, S2, B1 and S3, and for TSEB and TSEB-SM model, separately (R_n and G are forced to their measured value).

			TSEB			TSEB-SM		
			$RMSE$	R^2	MBE	$RMSE$	R^2	MBE
Using in-situ data	LE (W/m^2)	S1	109	0.39	76	**68**	**0.59**	**10**
		B1	136	0.15	165	**52**	**0.22**	**59**
		S2	86	**0.22**	30	72	0.16	-24
		S3	103	**0.53**	71	98	0.29	**-7**
	H (W/m^2)	S1	127	0.33	-41	**68**	**0.7**	**-10**
		B1	136	0.44	-165	**52**	**0.91**	**-59**
		S2	112	0.47	1	**72**	**0.63**	**24**
		S3	103	**0.38**	-71	98	0.14	**7**
Using satellite data	LE (W/m^2)	S1	95	0.34	119	**55**	**0.51**	**39**
		B1	66	**0.07**	181	**27**	0.01	**62**
		S2	67	0.02	94	**41**	**0.08**	**4**
		S3	56	0.55	128	**24**	**0.68**	**7**
	H (W/m^2)	S1	98	0.3	-104	**55**	**0.54**	**-39**
		B1	66	0.37	-181	**27**	**0.52**	**-62**
		S2	73	0.33	-71	**41**	**0.6**	**-4**
		S3	56	0.28	-128	**24**	**0.36**	**-7**

Table 5. Same as Table 2 but for simulated R_n and G.

			TSEB			TSEB-SM		
			$RMSE$	R^2	MBE	$RMSE$	R^2	MBE
Using in-situ data	Rn (W/m^2)	S1	35	0.99	-38	35	0.99	-38
		B1	14	0.99	12	14	0.99	12
		S2	20	0.99	9	20	0.99	9
		S3	**7**	0.99	-0.46	7	0.99	-0.46
	G (W/m^2)	S1	19	0.32	17	19	0.32	17
		B1	19	0.05	12	19	0.05	12
		S2	30	0.28	-13	30	0.28	-13
		S3	26	0.44	9	26	0.44	8
	LE (W/m^2)	S1	87	0.35	27	**65**	**0.58**	**-21**
		B1	141	0.12	174	**52**	**0.16**	**60**
		S2	91	**0.23**	35	**68**	0.22	**-15**
		S3	91	**0.62**	54	**84**	0.47	**22**
	H (W/m^2)	S1	127	0.33	-44	**70**	**0.73**	**34**
		B1	145	0.43	-177	**52**	**0.9**	**-60**
		S2	112	0.48	**2**	**78**	**0.68**	36
		S3	99	**0.3**	-64	**87**	0.3	**-32**
Using satellite data	Rn (W/m^2)	S1	23	0.94	8	22	0.93	8
		B1	85	0.47	32	85	0.47	32
		S2	22	0.94	12	22	0.94	12
		S3	17	0.97	2	17	0.97	2
	G (W/m^2)	S1	20	0.41	24	19	0.4	24
		B1	20	0	15	20	0	15
		S2	25	0.12	-15	25	0.12	-15
		S3	22	0.08	10	22	0.08	10
	LE (W/m^2)	S1	103	0.24	86	**52**	**0.49**	**28**
		B1	151	**0.02**	240	**30**	0.01	**65**
		S2	101	**0.07**	96	**37**	0.06	**28**
		S3	83	0.47	74	**24**	**0.69**	**14**
	H (W/m^2)	S1	112	0.34	-91	**63**	**0.44**	**-45**
		B1	150	0.16	-240	**28**	**0.49**	**-61**
		S2	97	0.4	-56	**38**	**0.52**	**-4**
		S3	85	0.12	-83	**27**	**0.28**	**-29**